Specialization in somatostatin subnetworks in sensory and association cortex

Christine F. Khoury[1,2], Noelle G. Fala[2], Caroline A. Runyan*[1,2]

[1]Center for the Neural Basis of Cognition, [2]Department of Neuroscience, University of Pittsburgh

*Corresponding Author: Caroline A. Runyan, runyan@pitt.edu

Abstract

Behavioral states profoundly affect cortical population activity dynamics and coding, yet the local circuits mediating these shifts are poorly understood, especially outside of sensory cortex. Somatostatin-expressing (SOM) inhibitory interneurons are highly sensitive to changes in brain state, and are well situated to modulate local population activity patterns. Here, we used two-photon calcium imaging to record the spike-related activity in populations of SOM and Non-SOM neurons in auditory cortex (AC) and posterior parietal cortex (PPC), to compare their functional interactions and activity modulation by behavioral state in sensory and association cortex. We have discovered both similarities and differences in the functional characteristics of SOM and Non-SOM populations across areas. In both regions, SOM neurons were more highly coordinated as populations than Non-SOM neurons. In PPC, SOM and Non-SOM neurons were positively modulated by increased arousal, while the effects of arousal in AC neurons were more diverse. Strikingly, the spatial structure of shared variability was different in AC and PPC: pairwise correlations in all cell types decayed rapidly with distance in AC but remained high over greater distances in PPC. Our results imply both generalization and specialization in the functional structure of excitatory and inhibitory subnetworks in sensory and association cortex.

Introduction

The mammalian neocortex is a hierarchically organized and highly interconnected network that can be subdivided into regions with functional specializations. Sensory cortices process incoming signals from single modalities, while downstream association areas integrate input from multiple modalities to generate behaviors. Incoming signals interact with rich, ongoing population activity dynamics throughout the brain, which are profoundly impacted by changes in behavioral and internal state.

The relationship between behavioral state and population activity dynamics has been most thoroughly explored in sensory cortex. In rodent sensory cortices, increased arousal has effects on cortical activity that are overall analogous to those of spatial attention in the primate visual system (1–5), including decorrelation of local population activity (6–9), enhanced response gain (10–14) and an improved signal:noise ratio (6, 13, 15). However, even across sensory cortices, the effects of arousal on neural activity are not uniform (16). For example, in auditory cortex (AC), but not other modalities, the effects of arousal are complicated by negative motor-related feedback from motor cortex through local inhibitory interneurons (8, 17, 18). Despite these differences, aroused and engaged behavioral states are associated with improved sensory

decoding across sensory cortices of multiple modalities. The circuits underlying these arousal-related effects are not fully understood, though inhibitory interneurons are likely to play important roles in controlling state-dependent shifts in population coding.

Inhibitory interneurons are critical components of local circuits, and well-situated to mediate many of the effects of internal state transitions on stimulus coding and population activity dynamics. The inhibitory cell class can be divided into three nonoverlapping subtypes, which express parvalbumin (PV), somatostatin (SOM), or vasoactive intestinal peptide (VIP), and participate in distinct local circuit motifs (19). Internal state transitions profoundly impact the activity of inhibitory interneurons. SOM neurons are particularly sensitive to internal state fluctuations, through direct activation of cholinergic and noradrenergic receptors (20–25), and through inhibition by VIP neurons (11, 26–30). In turn, SOM neurons can powerfully influence local networks, densely innervating the local excitatory population (26, 31, 32), sharpening stimulus selectivity and response reliability (33–35), modulating local population activity dynamics (22, 36), and flexibly modulating excitatory responses to stimuli based on behavioral relevance (37, 38).

The local-circuit functions of SOM neurons outside of sensory cortex remain largely uncharacterized, though the relative density of SOM to PV neurons is known to increase in association relative to sensory cortices (39, 40). Theoretical work suggests that this difference contributes to flexible coding properties of association cortex (38). Though many aspects of inhibitory microcircuitry are conserved across all of cortex, patterns of their synaptic connectivity and functional modulation by brain state may be tailored to specific regions' primary roles, such as in sensory processing or in performing flexible sensorimotor transformations.

Here, we tested the hypotheses that local inhibitory population activity in sensory and association cortex is differentially structured across neurons and differently modulated by arousal. We transgenically labeled SOM neurons in auditory and posterior parietal cortices and performed two-photon calcium imaging in both areas to relate SOM and Non-SOM activity to behavioral correlates of arousal, and to local population activity. We reveal clear area-specific differences in the modulation of SOM and Non-SOM neurons with changes in arousal. Furthermore, while the spatial scale of SOM and Non-SOM functional subnetworks differed in sensory and association cortex, commonalities in the activity relationships between SOM and other neurons were also evident across areas. Together, our results suggest that both specializations and generalized principles in the function of SOM neurons apply across cortex.

Results

To determine whether the effects of arousal on cell-type specific activity are conserved across sensory and association cortex, we compared spontaneous and sensory-evoked activity in auditory cortex (AC) and posterior parietal cortex (PPC) in six mice of both sexes. We used two-photon calcium imaging in superficial cortex to measure the spike-related activity of neurons positive and negative for the red fluorophore tdTomato, which was expressed transgenically in somatostatin-positive (SOM) neurons (41, 42). We virally expressed the genetically encoded calcium indicator GCaMP6f in all layer 2/3 neurons of AC and PPC in each mouse (43). Mice were head-fixed and ran voluntarily on a spherical treadmill; running velocity and pupil area were tracked throughout imaging sessions (Figure 1A-B).

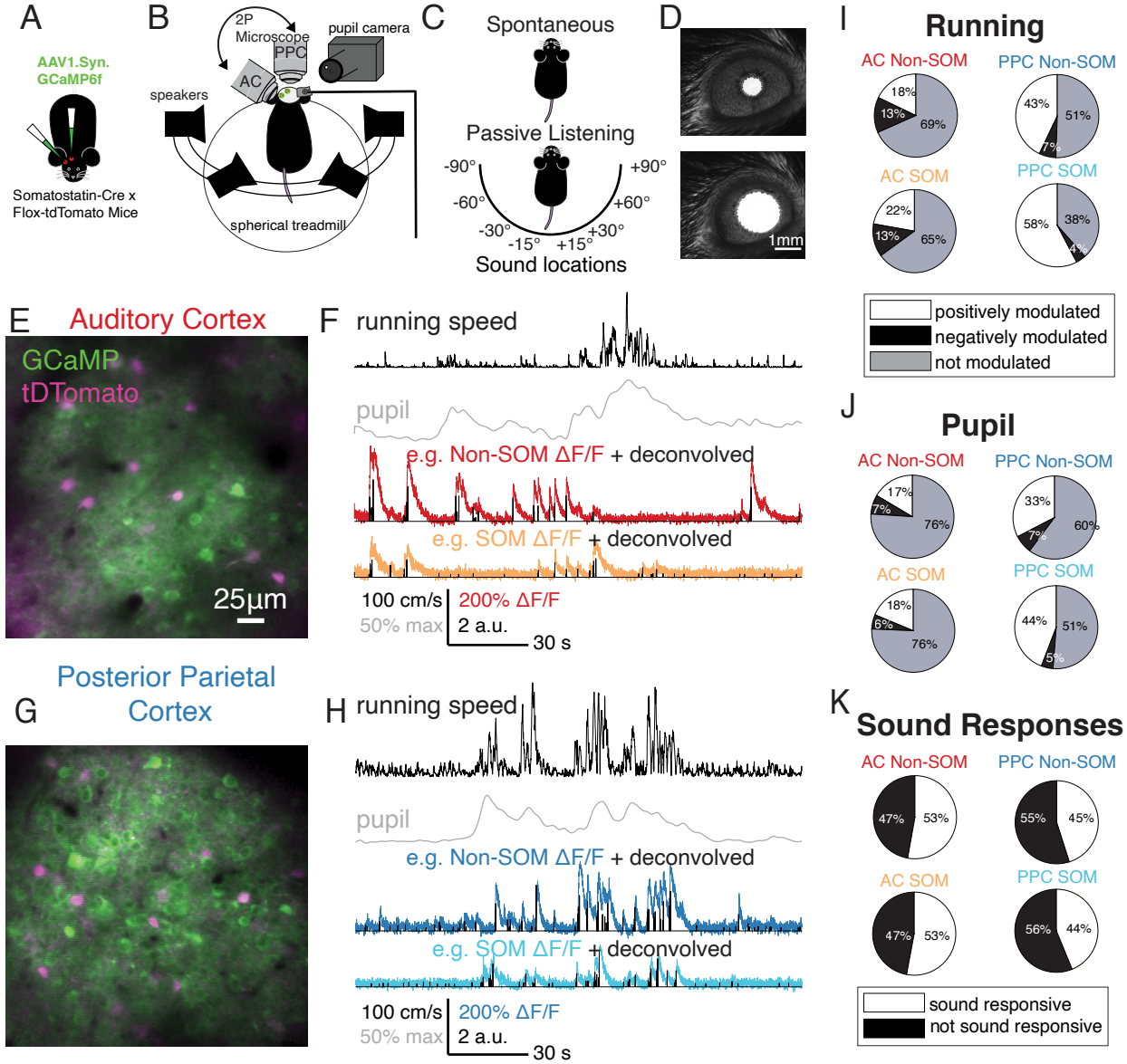

Figure 1: Imaging spike-related activity in SOM and Non-SOM neurons during behavioral state transitions. (A) Viral injections and cranial windows were made over auditory cortex (AC) and posterior parietal cortex (PPC) in each SOM-tdTomato mouse. (B) In imaging sessions, mice were headfixed over a spherical treadmill and allowed to run voluntarily. Four speakers arranged around the head presented sound stimuli. An infrared camera was used to image the pupil, and a rotating two-photon microscope was focused on either AC or PPC on a given imaging day. (C) Each imaging session included "Spontaneous" and "Passive Listening" contexts, without or with randomly presented sound stimuli from each of eight locations, respectively. (D) Pupil area was monitored via the pupil camera, scalebar in bottom image applies to top (constricted pupil) and bottom (dilated pupil). (E) Example field of view from auditory cortex, with intermingled tdTomato+/SOM+ (magenta) and tdTomato-/SOM- neurons, co-expressing GCaMP6f (green). (F) Example aligned behavioral and neural signals collected during the imaging session in E, including running speed (cm/s), normalized pupil area, dF/F from a Non-SOM (red) and SOM neuron (orange), each overlaid with the neuron's deconvolved estimated spike rates. (G) As in E, for an example posterior parietal cortex field of view. (H) As in F, for the PPC field of view in G. (I) Proportions of Non-SOM and SOM neurons in AC (left) and PPC (right) with significant positive (white), negative (black), or no modulation by mouse's running onset. AC Non-SOM N=2645; AC SOM N=359; PPC Non-SOM N=4719; PPC SOM N=525. (J) As in I, for pupil dilation. (K) Proportion of Non-SOM and SOM neurons in AC and PPC that were significantly sound responsive to at least one location (white) or not significantly sound responsive (black).

Behavioral state transitions differentially modulated neurons depending on cell-type and area

During each imaging session, we imaged AC or PPC during the "spontaneous" context, where the mouse ran freely on the spherical treadmill in the absence of sensory stimulation, and during "passive listening", where sounds were presented from eight separate locations (Figure 1B-C). We first examined how changes in pupil area and running speed corresponded with changes in activity of individual neurons during the spontaneous context. Throughout imaging sessions, mice spontaneously transitioned between behavioral states: stillness and running, and pupil constriction and dilation (Figure 1F, H, Figure S1A). To quantify the effect of behavioral state transitions on individual neurons' activity, we identified timepoints during the spontaneous context when either running speed or pupil area increased (Materials and Methods 5.2-5.3). The frequency of running bouts and dilation events was similar during PPC and AC imaging sessions ($p=.59$ and $p=.65$ respectively, Table S1). Mice initiated running bouts at a rate of .915±.095 (SEM) bouts per minute, and pupil dilations at .981±.070 (SEM) dilations per minute. Pupil area and running speed were higher during the passive listening context relative to the spontaneous behavior context (Figure S1).

To determine how transitions in behavioral state affected neural activity, we first quantified the effects of transitions from stationary to running on individual cells. We compared mean activity of each neuron (deconvolved estimated spike rates, here and throughout) in the 3-s time window following running bout onset to the 1-s time window prior to running bout onset (Figure 1I, See Materials and Methods 5.2). Pupil modulation was calculated similarly, based on transitions in pupil area from constricted to dilated (Figure 1D, J; Materials and Methods, 5.3). We compared each neuron's running and pupil modulation to shuffled distributions, where activity and behavioral data were time shifted by random intervals, and classified each neuron as positively, negatively, or not modulated by behavioral state transition. Larger proportions of the SOM and Non-SOM populations were modulated by both pupil dilations and running bout onsets in PPC than in AC (Figure 1I-J), suggesting that the effects of arousal on spontaneous neural activity are not uniform across areas.

Sound modulation of SOM and Non-SOM neurons' activity

To compare the auditory spatial selectivity of SOM and Non-SOM neurons in AC and PPC, sound stimuli (dynamic moving ripples) presented from eight distinct locations, centered on the mouse's head (Figure 1B-C, See Materials and Methods 3.4). We focused on spatial modulation of auditory stimuli due to PPC's role in spatial auditory processing during active behaviors (44). Sound responsiveness was determined similarly to pupil area and running speed modulation. We computed the mean difference in deconvolved activity during each sound presentation and the pre-stimulus period for each sound stimulus location, and compared to a shuffled distribution for each neuron (Materials and Methods 5.1). Large proportions of neurons in both areas were significantly sound responsive, but a greater proportion of AC SOM and Non-SOM neurons were sound responsive compared to PPC (53% of AC SOM and 53% of AC Non-SOM relative to 45% of PPC SOM and 44% of PPC Non-SOM neurons, Figure 1K), as expected.

Differing effects of arousal state on spontaneous activity of SOM and Non-SOM neurons in AC and PPC

To further characterize the relationship between arousal state transitions and spontaneous activity of single neurons in AC and PPC in the spontaneous context, we continued to focus on

128 “running bouts”, when the mouse’s running speed rapidly increased, to define behavioral state
129 transitions (Materials and Methods 5.2). We aligned and averaged the pupil area to running bout
130 onsets and observed that pupil area also increased during running bouts, though with a slower
131 time course (Figure 2A). We also aligned and averaged the activity of AC SOM, AC Non-SOM,
132 PPC SOM, and PPC Non-SOM populations (AC SOM and Non-SOM, n=24; PPC SOM and Non-
133 SOM, n=20 imaging sessions from 6 mice) to running bout onset (Figure 2A). While there was
134 little net change in the overall activity of AC populations relative to PPC, examining the activity of
135 each individual neuron revealed populations of SOM and Non-SOM neurons that increased or
136 decreased activity upon running onset. In PPC on the other hand, most Non-SOM and SOM
137 neurons increased activity at running onset (Figure 2B). We observed analogous results when
138 activity was aligned to transitions in pupil area (Figure S2A-B). While transitions in pupil area
139 corresponded with increases in running speed (Figure 2A, Figure S2A, D-E), the two signals
140 varied on different timescales. Running speed was characterized by a narrower autocorrelation
141 function than pupil area, demonstrating that running speed varied on a faster timescale than pupil
142 area (Figure S2C). To directly relate the two signals to each other, we computed the cross-
143 correlation between running speed and pupil area at different time lags. While the two signals
144 were highly correlated overall, the peak cross-correlation occurred at a 1.27s time lag, with
145 running preceding pupil area, further demonstrating the slower timescale of pupil changes relative
146 to running speed changes (Figure S2D).

147 Because of the slow time course of pupil area changes, we also characterized single neuron
148 activity during periods of sustained pupil constriction and dilation. We classified pupil
149 measurements as low, transitional, or high arousal states (Figure 2C, Materials and Methods 6.1),
150 and focused analyses on the low and high arousal states. As expected from the positive
151 correlation between running speed and pupil area, running speed was higher during the pupil-
152 defined high arousal than low arousal states ($p<.001$, Figure S2E). No running speed differences
153 were observed between AC and PPC imaging sessions in the high ($p=.087$) or low arousal
154 periods ($p=.89$). Mice ran on average 48.24±4.77 cm/s (SEM) during the high arousal state, and
155 7.71±1.29 cm/s (SEM) during the low arousal state (Figure S2E) and spent similar amounts of
156 time in the low and high arousal states during AC and PPC imaging sessions (Table S1).

157 Firing rates were elevated overall in high arousal states for SOM and Non-SOM neurons in both
158 regions ($p<.001$; Figure 2D-F, Table S2). To compare arousal modulation of activity in each
159 population of neurons, we next computed the Arousal Modulation Index (Materials and Methods
160 6.2), which could vary from -1 to +1, with -1 indicating greater mean activity in the low arousal
161 period, and +1 indicating greater activity in the high arousal period. The Arousal Modulation Index
162 differed significantly across the four groups (Figure 2G, $p<0.001$, Kruskal Wallis, Table S2).
163 Arousal modulation of PPC SOM and Non-SOM neurons was significantly greater than arousal
164 modulation of AC SOM and Non-SOM neurons ($p<.001$), but did not differ between AC SOM and
165 Non-SOM neurons ($p=.22$). In PPC, SOM neurons were significantly more modulated than Non-
166 SOM neurons ($p<.001$).

167 Finally, to consider the full time-varying relationship between ongoing neural activity and
168 behavioral correlates of arousal (running speed and pupil area), we correlated each neuron’s
169 activity and pupil area or running speed, across the entire spontaneous behavioral context
170 (Figure 2H-I). Pearson correlations between activity and pupil area/running speed were
171 significantly different across groups (pupil area and running speed, $p<0.001$, Kruskal-Wallis).
172 Consistent with the above analyses based on state transitions (Figures 1I-J, 2A-F), the

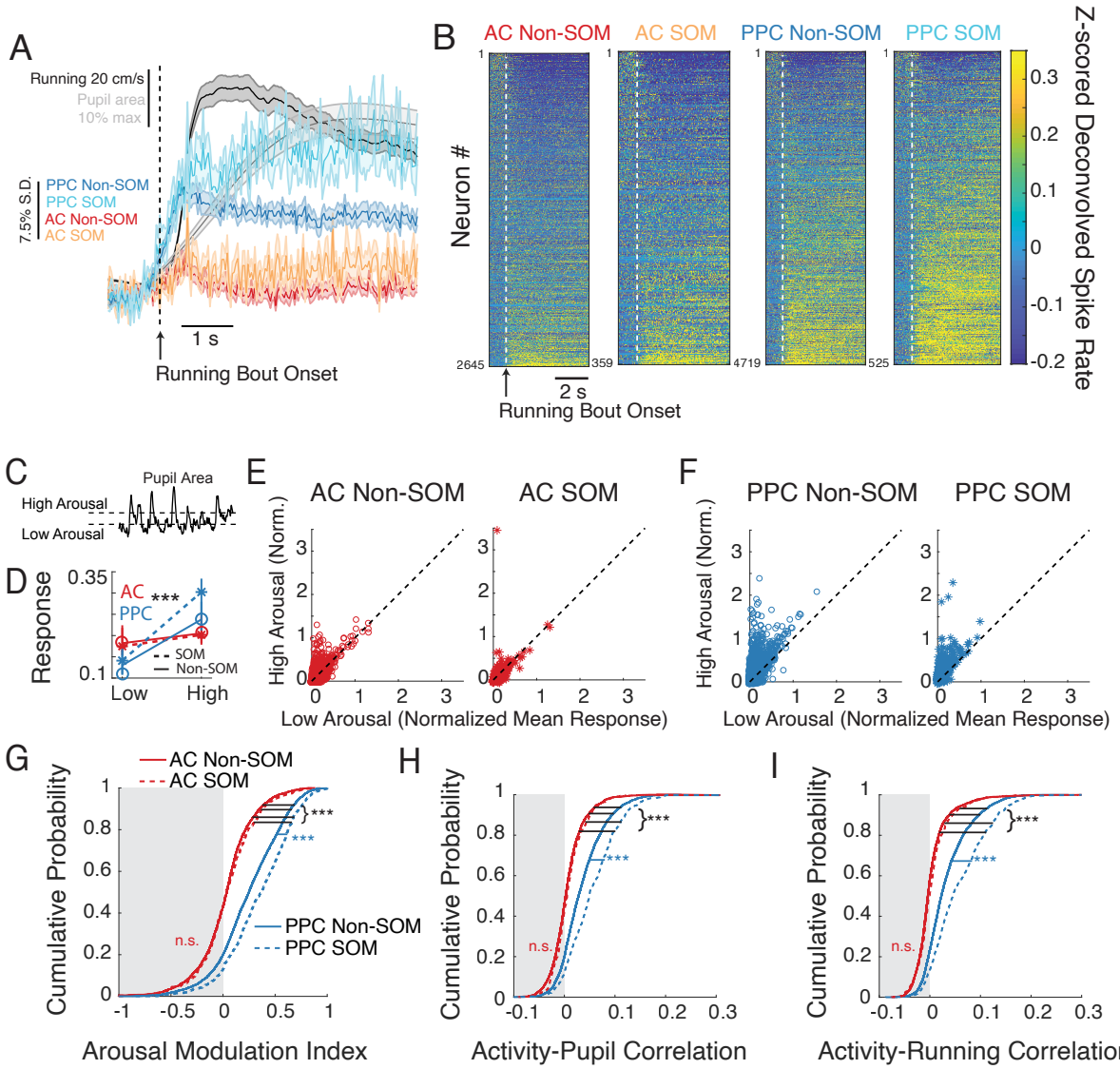

Figure 2: Single cell activity modulation with increases in arousal. (A) Average z-scored deconvolved activity, running speed, and pupil area aligned on running bout onset. Red: AC Non-SOM neurons' activity (N=24 datasets), Orange: AC SOM neurons' activity (N=24 datasets), Dark Blue: PPC Non-SOM neurons' activity (N=20 datasets), Light Blue: PPC SOM neurons' activity (N=20 datasets), Black: Running speed (N=44 datasets), Gray: Pupil area (N=44 datasets). (B) Average z-scored deconvolved activity of individual neurons, from L to R: all AC Non-SOM, AC SOM, PPC Non-SOM, and PPC SOM neurons aligned on running bout onset (AC Non-SOM N=2645; AC SOM N=359; PPC Non-SOM N=4719; PPC SOM N=525, in B-I). Neurons were sorted by running modulation. (C) Illustration of clustering that sorted pupil area during each imaging frame into low, transition, and high arousal states. (D) Mean responses of AC Non-SOM (red solid), AC SOM (red dotted), PPC Non-SOM (blue solid), and PPC SOM (blue dotted) neurons in low and high arousal states, as defined in C. (E) Left: Mean activity of AC Non-SOM neurons in high arousal state (classified with clustering as in C), plotted against mean activity in the low arousal state. Right: Mean activity of AC SOM neurons in high arousal vs low arousal states. (F) As in E, for PPC Non-SOM and SOM neurons. (G) Cumulative probability distribution of the arousal modulation index in AC Non-SOM (solid red), AC SOM (dotted red), PPC Non-SOM (solid blue), and PPC SOM (dotted blue) neurons. Arousal modulation index was calculated from the values in E-F, (High-Low)/(High+Low) for each neuron. (H) Cumulative probability distribution of the Pearson correlation between each neuron's activity and pupil area, colors as in G. (I) Cumulative probability distribution of the Pearson correlation between each neuron's activity and running speed. Significance as indicated, permutation test, *** p<.001. Error bars: 95% bootstrapped confidence interval around the mean. See full summary of values and statistics in Tables S2-3.

correlations between activity and running/pupil size were significantly greater in PPC SOM and Non-SOM neurons than AC SOM and Non-SOM neurons ($p<.001$). In AC, SOM and Non-SOM neurons were similarly correlated to running/pupil size (pupil, $p=.063$, running, $p=.146$), while in PPC, SOM neurons were significantly more correlated with both running and pupil than were Non-SOM neurons ($p<.001$, Figure 2H-I, Table S3).

Taken together, our results indicate that SOM and Non-SOM neurons have heterogeneous activity relationships with arousal state in AC, whether defined by running speed or pupil area. In PPC, on the other hand, neural activity was strongly and positively related to increased arousal. In AC, no differences in arousal-modulation of SOM and Non-SOM neurons were evident, while in PPC, SOM neurons were more sensitive to increases in arousal than Non-SOM neurons. All analyses reported in Figure 2 used data collected during the spontaneous context to isolate the effects of arousal on spontaneous activity in the absence of sensory evoked responses. However, we obtained analogous results using data collected during the passive listening context, suggesting that the overall effects of arousal are similar with and without sensory stimulation (Figure S3, Tables S4-5).

An encoding model to disentangle running speed and pupil size contributions to single cell activity

Running speed and pupil area are strongly correlated signals but do vary on different timescales (Figure S2C-D) and have separable impacts on neural activity (6). Our analyses of ongoing spontaneous activity in AC and PPC hint at the possibility of separable effects of pupil area and running speed, as AC Non-SOM neurons' activity was more highly correlated with pupil area ($0.0057\pm.00063$ SEM) than with running ($.0020\pm.00066$ SEM, $p<.001$).

To disentangle the relationships between neural activity, running speed, and pupil area, we used a generalized linear modeling (GLM) approach (45–47). We constructed an encoding model (GLM), that used sound stimulus timing and location, pupil area, and running velocity to predict the responses of individual SOM and Non-SOM neurons in AC and PPC, in the passive listening context (Figures 3A, S4). It should be noted that in the above analyses (Figure 1I, 2A-B,2I), we considered only the speed at which the mouse was running in any direction, as increased running speed is correlated with heightened arousal (6, 8, 11, 12, 14, 16). Because PPC neurons' activity can be selective for running direction (45, 48–51), in the GLM we used running velocity rather than speed to obtain more accurate predictions for each neuron (Materials and Methods 8.0, Figure S4).

To determine the relative contributions of pupil area and running velocity to neurons' activity, we compared the prediction performance of variants of the model that were missing either predictors based on pupil area or running velocity to the prediction performance of a model that included pupil area, running velocity, and sound stimulus predictors (Figure 3). For each neuron, we calculated running and pupil area contributions to its activity as the difference between the performance of the full model and the no-running and no-pupil models respectively (Materials and Methods 8.6). This approach allowed us to isolate the contributions of running velocity and pupil size that were not redundant with each other. For example, when pupil area is well-explained by running velocity, running predictors would account for the missing pupil area predictors, and the performance of the model would not be degraded compared to the full model that includes both pupil area and running velocity predictors. The model comparison revealed single neuron activity that could be explained uniquely by running and by pupil in both AC and PPC (Figure 3B-G, note

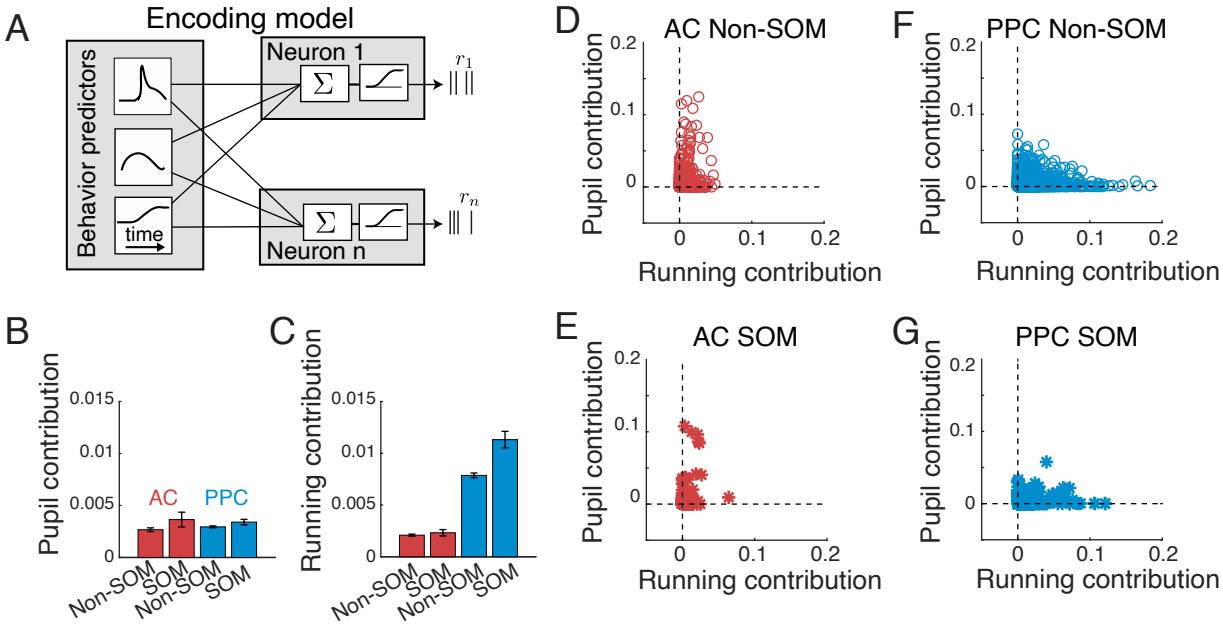

Figure 3: Using an Encoding Model to Disentange Running and Pupil Contributions to Single Cell Activity. (A) Schematic of Generalized Linear Model (GLM) used to determine contributions of pupil area and running velocity to neurons' activity. (B) Average contribution of pupil area to activity across all AC Non-SOM (N=2645) and SOM (N=359) neurons (red bars) and PPC Non-SOM (N=4525) and SOM (N=505) neurons (blue bars). Contribution was quantified as the improvement in model prediction performance of each neuron's activity when adding pupil area as a set of predictors. Errorbars indicate SEM (C) As in B, calculated when comparing model performance with and without running velocity predictors. (D) Pupil contribution plotted against running contribution for each AC Non-SOM neuron, calculated as in B. (E) Pupil contribution plotted against running contribution for each AC SOM neuron. (F-G) Pupil contribution plotted against running contribution for each PPC Non-SOM or SOM neuron. Sample sizes in B apply to all panels, full statistics in Table S6.

neurons along the pupil and running contribution axes in D-G). Contributions of pupil size to activity were slightly stronger in PPC than AC overall ($p<0.05$, Table S6). Running contributions were stronger overall in PPC neurons than AC neurons ($p<0.001$), and even higher among PPC SOM neurons than PPC Non-SOM neurons ($p<0.001$ Figure 3C, F, G, Table S6). The elevated running velocity contribution in PPC neurons is consistent with PPC's role in sensorimotor transformations and navigation (45, 52, 53).

Characterizing sound location responses from AC and PPC in low and high arousal

To characterize sound location specificity of responses in AC and PPC, we computed a location selectivity index (LSI, Figure S5A-D, See; Materials and Methods 10.0). PPC neurons overall were less selective for location than AC neurons ($p<0.01$, Table S7), and PPC sound responses were less reliable ($p<0.001$, Table S8). Within both regions, Non-SOM neurons were more selective for sound location than SOM neurons ($p<0.001$, Figure S5B-C, Table S7). Based on the differences in location selectivity and response reliability, we expected population activity to represent sound location more accurately in AC than PPC.

We built decoders based on population activity that predicted the most likely sound stimulus location using the activity of subsets of neurons ("best cells", SOM neurons, or Non-SOM neurons). The number of neurons was matched for sample size across cell types for valid comparisons of population decoding performance. Each decoder was based on a Bayesian inversion of our encoding model (Figure 4A, Materials and Methods, 9.0). The posterior probability of each stimulus ($p(s|r)$, where s is the stimulus and r is the response probability of the simultaneously imaged neurons) was then computed cumulatively at each timepoint using all previous timepoints in the trial. Decoder performance was quantified as the fraction of trials where the stimulus with the maximal posterior probability matched the actual presented stimulus.

First, to compare the overall ability of AC and PPC to represent sound location, we used activity of only the "best" cells (i.e., individual neurons with the best sound location decoding themselves) regardless of cell type in the population decoder. The best cell decoder's performance was above chance when using activity from both AC and PPC (Figure 4C-D, Materials and Methods, 9.0). However, as expected, AC decoding was more accurate than PPC decoding ($p<0.001$; Figure 4C-D, Materials and Methods 9.0, Table S9). Next, to compare sound location decoding accuracy in the SOM and Non-SOM populations, we built population decoders based on n-matched populations of SOM and Non-SOM neurons from each dataset. In both areas, sound location decoding was similar in SOM and Non-SOM populations (Figure 4C), and both cell type populations from AC outperformed decoding based on PPC populations ($p<0.001$, Figure 4C-D). All cell-type specific, subsampled population decoders performed significantly worse than the decoders based on an n-matched population of "best" neurons ($p<0.001$; Figure 4D, See Materials and Methods 9.0). The same was true when instead of decoding left or right, we decoded specific contralateral sound locations (Figure S6). To summarize, sound location was better represented in AC than PPC, and SOM and n-matched Non-SOM populations in both areas were similarly informative about sound location. A sparse code for sound location was evident in both AC and PPC, as small numbers of highly tuned "best" neurons more accurately encoded sound location than random subsamples of the population.

To determine how arousal-related activity modulation affects sensory representations in AC and PPC, we also trained and tested decoders in low and high arousal periods. Sound stimulus trials

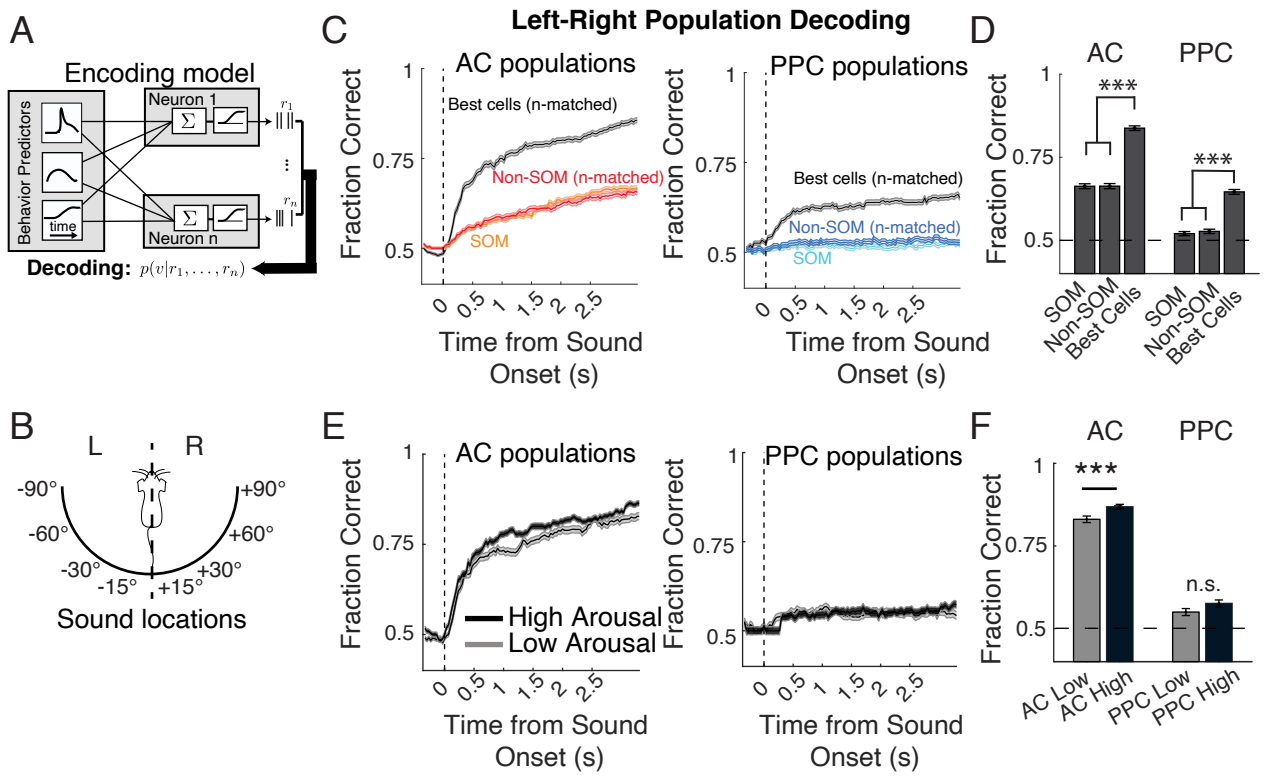

Figure 4: Decoding Sound Location from AC and PPC Population Activity. (A) The encoding model was trained on all trials that included all arousal levels, and inverted using Bayes Rule to compute the posterior probability of auditory stimuli given the activity of the neural population in AC and PPC . (B) Schematic of the discrimination being performed by the decoder, classifying sound stimuli as occuring from the left or right of the mouse. (C) Left: Mean cumulative population decoder performance (across datasets) when classifying left vs right locations, when based on "best cells", defined as individual Non-SOM cells or SOM cells with the highest decoding performance. "Best cells" and Non-SOM cells in each dataset were subsampled to match the N of the SOM neuron population within each imaging field of view. Right: Population decoder performance using PPC neurons. Chance performance is 0.5. (D) Mean decoder performance using all timepoints in the trial (equivalent to the final timepoints in (C) using SOM neurons, subsampled Non-SOM neurons, and "best cells" in AC and PPC. Dotted line corresponds to chance performance (50%). (E) Mean fraction correct of cumulative sound location (left sound locations vs right sound locations) decoding in AC (right) and PPC (left) populations in high (dark) and low (light) arousal conditions. Subsampling to match arousal and sound locations was repeated 10x. (F) Cumulative fraction correct of decoding for left vs right sound location at the end of the trial in AC and PPC. Shading in C,E and errorbars in D,F indicate SEM, *** p<0.001, n.s. not significant. AC Non-SOM N=24 datasets; AC SOM N=24 datasets; PPC Non-SOM N=20 datasets; PPC SOM N=20 datasets throughout figure panels. See Table S9 for full statistics.

were classified as occurring during low or high arousal based on the pupil area states (Materials and Methods, 6.1, Figure 2C), and low and high arousal trials were evenly balanced to train and test the decoders. Decoding performance for left vs. right sound location category using AC populations was modestly improved during heightened arousal, but decoding performance was similarly poor in low and high arousal trials using PPC populations (Figure 4E-F, Table S9). Thus, while generalized arousal seems to improve sensory coding in AC, it had no impact on coding within PPC populations.

To summarize our analyses characterizing the relationship between neural activity, sensory stimuli, and behavioral state, heightened arousal led to modest net increases in overall activity in AC SOM and Non-SOM populations, and more pronounced and uniform increases in activity across neurons in PPC. SOM neurons in PPC were most strongly modulated by behavioral state. Still, sensory coding only improved in AC, but not PPC, during periods of high arousal. Critically, cortical circuits are comprised of interdependent, highly interconnected neurons that share common input (31, 59–63), and the resulting ongoing population activity patterns interact with incoming signals related to behavioral state or sensory stimuli (64). Interactions among excitatory and inhibitory neurons, such as SOM neurons, are important for setting and maintaining the dynamics of ongoing population activity (22, 36, 65).

In the following sections, we compare the interactions of SOM and Non-SOM neurons with each other in AC and PPC.

Noise correlations were strongest within SOM populations in both AC and PPC

Task engagement, attention, and arousal also impact neural activity at the population level, reducing shared variability in sensory cortex (1, 2, 6–9, 22). Correlated variability is higher in PPC than in AC, allowing PPC populations to encode information more stably over time, and improving readout of perceptual choices by downstream regions (45, 66). The local circuit mechanisms contributing to these differing population activity patterns in AC and PPC are not known, but are likely to involve inhibitory interneurons, which can modulate population activity coherence (22, 36).

The arousal-related shifts in SOM activity, especially in PPC, demonstrated here lead to the question of how SOM neuron activity co-fluctuates with other neurons in the local population. As expected from our previous work (45), pairwise correlations overall were lower in AC than in PPC ($p<.001$, Table S10). Noise correlations also tended to be weaker in the high arousal states, but the effect depended on signal correlation, area, and cell type (Figure S7, Table S11). To characterize the patterns of functional interactions within and between cell types, we measured the pairwise noise correlations between Non-SOM/Non-SOM pairs, SOM/SOM pairs, and Non-SOM/SOM pairs (Figure 5A-C). In both regions, noise correlations differed across these three cell type combinations (AC: Kruskal Wallis, $p<.001$; PPC: Kruskal Wallis, $p<.001$). In both AC and PPC, SOM/SOM correlations were higher than both Non-SOM/Non-SOM correlations ($p<.001$) and Non-SOM/SOM correlations ($p<.001$, Table S10). Despite the lack of monosynaptic connections among SOM neurons (26), the high SOM/SOM noise correlations in both regions support the idea of functional subnetworks of SOM neurons in local cortical circuits (67).

The spatial scale of functional connectivity differed in AC and PPC

To characterize the spatial extent of pairwise noise correlations in AC and PPC, we related mean pairwise correlations to inter-somatic distance (Figure 5D-G). Within 100 µm, correlations between Non-SOM/Non-SOM pairs were similar across regions (Figure 5D-E, Table S12). However, at longer distances, AC pairwise correlations decayed rapidly, while PPC pairwise correlations remained relatively elevated across all distances (Figure 5D-F). SOM/SOM pairwise correlations remained higher in PPC than AC across all inter-somatic distances ($p<.001$, Figure 5F, Table S12).

To quantify the rate of decay in pairwise correlations over cortical distance, we fit an exponential equation to determine the decay constant lambda (λ) , across binned pairwise distances (Materials and Methods 7.3). The spatial decay was faster in AC than PPC for all cell type combinations (Figure 5G, $p<.001$, Table S13). The spatial patterns of noise correlations were similar when calculated based on running bout "trials" rather than sound stimulus presentations (Tables S14-16, Figure S8).

Together, the noise correlation analyses revealed both similarities and differences in the structure of functional correlations between cell types across cortex. SOM neurons tended to be more strongly correlated with each other than with other neurons in both AC and PPC. Within AC, noise correlations were highest at close pairwise distances but decayed rapidly with distance. Within PPC, pairwise correlations remained elevated across distances over 300 µm, with SOM-SOM correlations remaining highest across distance. These results suggest differences in the spatial scales of functional SOM subnetworks in AC and PPC (Figure 5H), which may allow SOM neurons in PPC to pool excitation over overlapping, wider distances, and act as a more coordinated population in PPC than in AC (Figure 5H).

Functional coupling within SOM populations remained higher in both AC and PPC after discounting behavioral and sensory influences

The noise correlation results (Figure 5) suggest important similarities and differences in the structure of functional SOM subnetworks in AC and PPC. However, pairwise noise correlations cannot easily discount the effects of ongoing fluctuations in sensory stimuli and behavioral variables such as running direction, speed, and pupil size, which modulate AC and PPC SOM and Non-SOM activity differently (Figures 1-3) (14, 17, 45). To measure correlated variability while accounting for sensory stimuli and behavioral variables, we returned to the generalized linear model (GLM) approach, to compute the level of "coupling" among SOM and Non-SOM neurons in AC and PPC in isolation of common drive from behavioral or sensory-related inputs (45, 46). The coupling measurement shares the goal of noise correlation analyses, while discounting many time-varying behavioral correlates simultaneously. Furthermore, coupling measurements can also measure high order co-fluctuations between multiple neurons, beyond the pairwise relationships measured with noise correlations (46).

Our approach to measuring coupling is analogous to the approach we used to determine the running velocity and pupil area contributions to each neuron's activity. We again trained and tested variants of the encoding model and compared their prediction performance of each neuron's activity. The uncoupled model included time varying predictors based on running velocity, pupil area, and sound stimulus presentation. The coupled variants of the model included

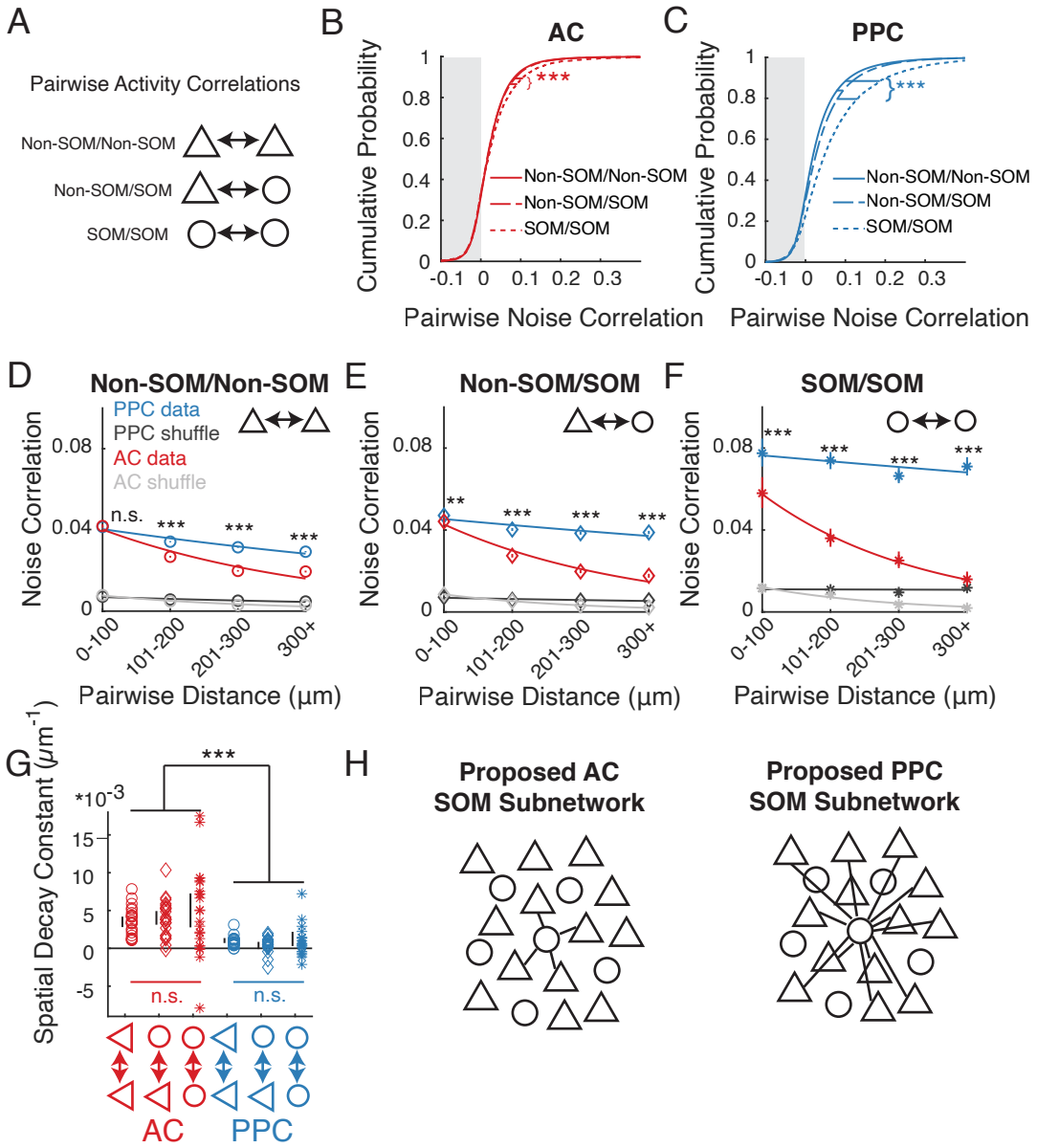

Figure 5: The Spatial Scale of Correlated Variability Differs in AC and PPC. (A) The pairwise correlations considered in following analyses. (B) Cumulative probability distributions of the noise correlations in Non-SOM/Non-SOM pairs (N=160241), Non-SOM/SOM (N=41473), and SOM/SOM (N=2788) pairs in AC. SOM/SOM correlations were higher on average than other cell type pairs. (C) As in B, for PPC neurons (Non-SOM/Non-SOM, N=620319; Non-SOM/SOM, N=129319; SOM/SOM, N=7644). Similar to AC, SOM/SOM pairs tended to be more correlated. (D) Mean pairwise noise correlations of Non-SOM/Non-SOM neurons binned by intersomatic distance in AC (red) and PPC (blue). n.s.: no significant difference; *p<.05; **p<.01; ***p<.001. Points indicate mean, lines are 95% bootstrapped confidence intervals of the mean. (E) As in D for Non-SOM/SOM pairs. (F) As in D-E for SOM/SOM pairs. (G) Lambda, the decay constant of a single exponential function fit to the correlation vs. distances in D-F. n.s.: No significant differences in the decay constant within regions. Each point represents the lambda values for one pair type from one dataset, black lines show 95% bootstrapped confidence interval of the mean. AC N=24 datasets; PPC, N=20 datasets. (H) We propose that the spatial scale of excitatory-SOM networks is wider in PPC than in AC, explaining the differences in spatial decay of functional coupling among SOM neurons across areas. Full summary of values and statistics presented here available in Supplementary Tables 10, 12-13.

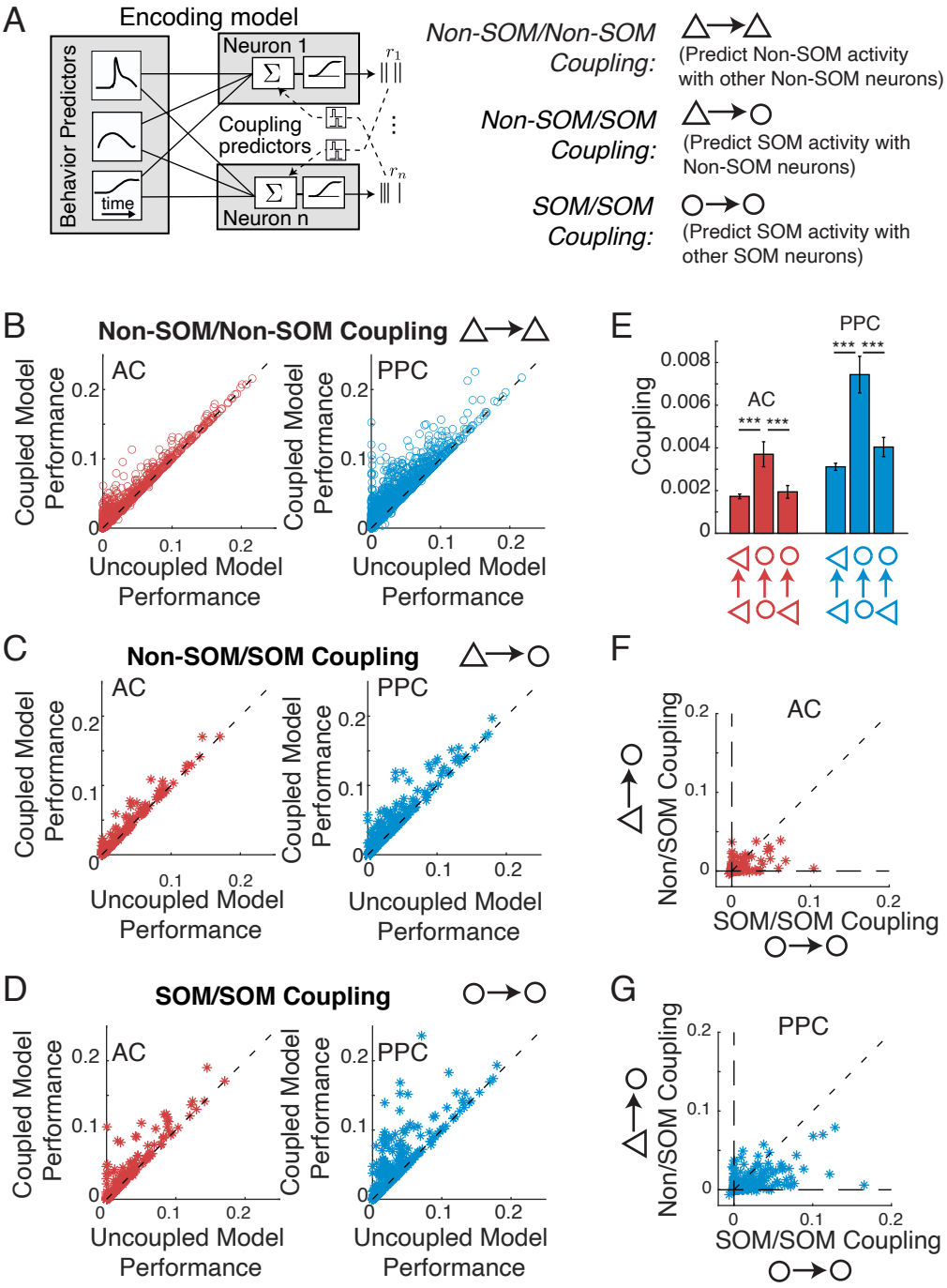

Figure 6: Functional Coupling is Highest between SOM Neurons. (A) Left: Schematic of the Generalized Linear Model (GLM) used to measure functional coupling between neuron types. Behavioral predictors and coupling predictors from either SOM or Non-SOM neurons were used to predict each neuron's activity. Right: Types of coupling assessed. (B) Performance improvement when adding Non-SOM coupling to the model to predict activity of Non-SOM neurons in AC (left, N=2428) and PPC (right, N=4048) neurons. X axis: uncoupled model prediction performance (fraction of deviance explained). Y axis: coupled model prediction performance, using Non-SOM neurons as coupling predictors. (C) As in B, when using Non-SOM neurons to predict each SOM neuron's activity (AC, N=320; PPC, N=485). (D) As in B-C, when using SOM neurons to predict each SOM neuron's activity (AC, N=320; PPC, N=485). (E) Mean coupling (Model performance improvement when adding coupling: Y-axis minus X-axis for each neuron in B-D), measured with the three coupled model types in AC (red bars) and PPC (blue bars) neurons. (F) Comparison of Non-SOM and SOM coupling to SOM neurons in AC. (G) As in F, for PPC SOM neurons. Error bars indicate SEM, *** p<0.001. Full summary of values and statistics in Supplementary Table 17.

these in addition to predictors based on the activity of subsets of the simultaneously imaged neurons: the “SOM coupled model” used the activity of SOM neurons in the field of view as predictors, and the “Non-SOM coupled model” used the activity of a subsampled population of Non-SOM neurons, chosen to match the size and distance distribution of the SOM population within that field of view.

We calculated each neuron’s coupling to the SOM population by subtracting the single trial prediction performance of the uncoupled model (fraction deviance explained, compared to the null model) from the prediction performance of the SOM coupled model, using data that had not been used to train the model. Similarly, each neuron’s Non-SOM coupling was calculated by subtracting the performance of the uncoupled model from the performance of the Non-SOM coupled model (Materials and Methods 8.0, Figure 6A). This approach allowed us to isolate functional coupling of each neuron to local SOM and Non-SOM subpopulations that could not be explained by sound stimuli, running behavior, and pupil area fluctuations (i.e., the difference in the y and x axes for each neuron in Figure 6B-D).

We calculated three types of coupling: 1) Non-SOM/Non-SOM (Figure 6B); 2) Non-SOM/SOM coupling (Figure 6C); and 3) SOM/SOM coupling (Figure 6D). As expected from previous results (Runyan et al., 2017), coupling among Non-SOM neurons was higher in PPC than AC ($p < 0.001$, Figure 6E). Coupling among SOM neurons was also higher in PPC than in AC ($p < 0.001$), as was Non-SOM/SOM coupling ($p < 0.001$). Consistent with noise correlations (Figure 5A-C), coupling among SOM neurons was higher than coupling between other cell types in both AC and PPC ($p < 0.001$, Figure 6E-G, Table S17).

In summary, even when accounting for co-modulation of neural activity by changes in running speed, pupil size, and sound stimulation, coupling among neurons was high in PPC relative to AC, and coupling among SOM neurons was higher than coupling among other cell types within both regions.

Discussion

To compare the functional structure of inhibitory subnetworks across cortex, we have measured the spike-related activity in populations of somatostatin-expressing inhibitory interneurons (SOM) and Non-SOM neurons in auditory cortex (AC) and in posterior parietal cortex (PPC), while mice experienced spontaneous arousal shifts. We examined the impact of these shifts on ongoing activity patterns, as well as on sound-evoked responses. Our results reveal both common principles in the functional structure of SOM and Non-SOM population activity, as well as region-specific differences, implying some specialization in the function of SOM neurons across sensory and association-level cortices.

In AC, where spontaneous population activity was decorrelated overall compared to PPC, the effects of arousal on individual neurons were diverse, with only a small net positive effect on population activity. In PPC, increases in arousal led to a general increase in activity across most neurons. In AC, SOM and Non-SOM populations showed similarly diverse arousal-related responses, while in PPC, SOM neurons were even more strongly activated with increased arousal than Non-SOM neurons. Although increases in running speed and pupil size were strongly related to each other, we were able to disentangle the contributions of running velocity and pupil size to the activity of individual neurons in AC and PPC using an encoding model (Figure 3). In both regions, pupil size and running velocity contributed to the activity of SOM and

Non-SOM neurons. However, more of the arousal-related activity modulation in PPC was explained by changes in running velocity, while in AC, pupil size and running velocity were similarly weak contributors to activity. This is likely related to PPC's role in navigation and sensorimotor transformations (45, 47, 51–53, 57, 68).

The effects of arousal on neural activity and coding have been examined in depth across primary sensory cortices. Overall, our results are consistent with this body of work, which has revealed a relationship between correlated variability and arousal state (6–9). In primary auditory cortex, the Yerkes-Dodson (inverted-U) relationship between pupil size and sound decoding has been observed (9, 14), which aligns well with the known links between norepinephrine levels and behavioral performance and an "optimal" level of arousal for behavioral performance (69). We did not observe this effect, instead measuring a modest improvement in decoding accuracy with arousal. Mice in our experiments were most likely to visit two separable behavioral states (stationary/unaroused or running/aroused), without the gradation of different levels of arousal observed by others. Our "high" arousal state likely includes a mixture of the moderate and high arousal states defined by others when three separable states can be identified. It is important to note that while locomotion, whisking, and pupil dilations have all been considered as behavioral correlates of an animal's arousal state, motor-related feedback acts on specialized circuits within visual, somatosensory, and auditory cortices (11, 17, 18, 70–72) that interact with neuromodulatory inputs, leading to different arousal-related effects on network activity in those regions. It is unlikely that any aroused state is without a related change in fidgeting, facial movements, or other motor outputs (73, 74).

In general, activity within the SOM subpopulation was more coordinated in both AC and PPC, compared to the Non-SOM population, which includes mostly excitatory neurons. This is consistent with previous findings within primary visual cortex, in which shared variability is overall higher within inhibitory cell types than between types (67, 75, 76). Our similar results in sensory and association cortex indicate it is likely a general property of the somatostatin population across cortical areas, despite differences in overall correlated variability between the two regions. Despite this similarity in cell-type specific activity relationships in AC and PPC, the spatial scales of functional interactions between neurons differed markedly in the two regions. In AC, pairwise correlations decayed rapidly with distance (Figure 5), as has been well established in sensory cortex (77–82). In contrast, pairwise noise correlations remained high over longer distances in PPC, suggesting a different spatial structure of correlated variability in association cortex, consistent with findings in primates (83). SOM/SOM noise correlations, which were stronger overall than Non-SOM/Non-SOM correlations, remained high across all measured distances in PPC. Given the role for SOM neurons in providing lateral inhibition by pooling excitatory inputs and inhibiting neighboring neurons (33, 84), we suspect that the wider spatial scale of SOM/SOM activity correlations in PPC implies that SOM neurons receive excitatory synapses from farther distances in PPC than in AC (Figure 5H). Future work will determine whether this is the case, and whether the magnitude and spatial scale of correlated variability, particularly within SOM subnetworks, increases systematically across the cortical hierarchy.

Taken together, our results demonstrate key differences in the spatial extent of coordinated inhibitory subnetworks across cortex, as well as in arousal-related modulation of activity dynamics, adding to a growing body of evidence that cortical microcircuits are functionally specialized across cortical regions (39, 40, 45). The role of distinct cortical areas in processing incoming sensory information or generating behaviors varies across cortex, and the underlying

431 spatial patterns and dynamics of population activity may be tailored to these specialized roles.
432 Primary sensory areas, such as AC, encode fine-grain details time-varying sensory stimuli, and
433 are organized topographically. Meanwhile, multisensory inputs converge in association-level
434 regions such as PPC, which then flexibly integrates sensory information over time and transforms
435 it to influence behavioral choices (45, 57, 58, 85, 86). The flexible, task-dependent integration of
436 diverse feedforward signals in PPC may require larger scale network dynamics, as we observed
437 in SOM and Non-SOM populations.

438 **Materials and Methods**
439
440 **1.0 Statistics**

441 All pairwise comparisons were done with two-sided paired or unpaired permutation (i.e.
442 randomization) tests with 10,000 iterations as indicated, where p<.0001 indicates the highest
443 significance achievable given the number of runs performed. All permutation tests were
444 performed for differences in means. For statistical comparisons involving more than two groups,
445 we used Kruskal-Wallis (non-parametric ANOVA) and used unpaired permutation tests post-hoc
446 to determine which groups differed from each other. Data fell into natural groupings by 1) brain
447 area (AC or PPC) and by 2) cell-type (SOM or Non-SOM), as indicated by expression of the red
448 fluorophore, tdTomato. All bar plots show mean and bootstrapped 95% confidence intervals
449 unless otherwise indicated. When multiple comparisons were made between groups, p values
450 were Bonferroni-corrected. Sample sizes were chosen based on previous studies comparing
451 population activity dynamics across brain areas or cell types (45, 76).

452 **2.0 Animals**

453 All procedures were approved by the University of Pittsburgh Institutional Animal Care and Use
454 Committee. Homozygous SOM-Cre mice (Sst-IRES-Cre, JAX Stock #013044) were crossed with
455 homozygous Ai14 mice (RCL-tdT-D, JAX Stock #007914) obtained from Jackson Laboratory, ME,
456 USA, and all experiments were performed in the F1 generation , which expressed tdTomato in
457 SOM+ neurons. Mice were group housed in cages with between 2 and 4 mice. Adult (8-24
458 weeks) male and female mice were used for experiments (4 male, 2 female). Mice were housed
459 on reversed 12 hr light/dark cycle, and all experiments were performed in the dark (active) phase.

460 *2.1 Surgical procedures*

461 Mice were anesthetized with isoflurane (4% for induction, and 1-2% maintenance during surgery),
462 and mounted on a stereotaxic frame (David Kopf Instruments, CA). Ophthalmic ointment was
463 applied to cover the eyes (Henry Schein, NY). Dexamethasone was injected 12-24 hours prior to
464 surgery, and carprofen and dexamethasone (Covetrus, ME) were injected subcutaneously
465 immediately prior to surgery for pain management and to reduce the inflammatory response. Two
466 2 x 2 mm craniotomies were made over left AC (centered at 3.0 mm posterior and 4.3 mm lateral
467 to bregma) and PPC (centered at 2 mm posterior and 1.75 mm lateral to bregma). 1-4 evenly
468 spaced ~60 nl injections of AAV1-synapsin-I-GCamp6f (Addgene, MA stock #100837) that had
469 been diluted to a titer of ~1x10^12 vg/mL using sterile PBS were made in each cranial window,
470 centered on the same coordinates listed above. A micromanipulator (QUAD, Sutter, CA) was
471 used to target injections ~250 µm under the dura at each site, where ~60 nl virus was pressure-
472 injected over 5-10 minutes. Pipettes were not removed until 5 minutes post-injection to prevent
473 backflow. Dental cement (Parkell, NY) sealed a glass coverslip (3mm) over a drop of Kwik Sil

474 (World Precision Instruments, FL) over the craniotomy. Using dental cement, a one-sided titanium
475 headplate was attached to the right hemisphere of the skull. After mice had recovered from the
476 anesthesia, they were returned to their home cages, and received oral carprofen tablets (Bio-
477 Serv, NJ) for 3 days post-surgery.

478 **3.0 Experimental Setup**

479 *3.1 Two-photon microscope*

480 Images were acquired using a resonant scanning two-photon microscope (Ultima Investigator,
481 Bruker, WI) at a 30 Hz frame rate and 512 x 512 pixel resolution through a 16x water immersion
482 lens (Nikon CF175, 16X/0.8 NA, NY). On separate days, either AC or PPC was imaged at a
483 depth between 150 and 300 µm, corresponding to layers 2/3 of cortex. For AC imaging, the
484 objective was rotated 35-45 degrees from vertical, and for PPC imaging, it was rotated to 5-15
485 degrees from vertical, matching the angle of the cranial window implant. Each field of view
486 contained approximately 100-300 neurons total, and 5-30 SOM neurons. Excitation light was
487 provided by a femtosecond infrared laser (Insight X3, Spectra-Physics, CA) tuned to 920 nm.
488 Green and red wavelengths were separated through a 565 nm lowpass filter before passing
489 through bandpass filters (Chroma, ET525/70 and ET595/50, VT). PrairieView software (v5.5,
490 Bruker, WI) was used to control the microscope.

491 *3.2 Behavioral monitoring*

492 Running velocity was monitored on pitch and roll axes using two optical sensors (ADNS-98000,
493 Tindie, CA) held adjacent to the spherical treadmill. A microcontroller (Teensy, 3.1, Adafruit, NY)
494 communicated with the sensors, demixing their inputs to produce one output channel per
495 rotational axis using custom code. Outputs controlling the galvanometers were synchronized with
496 running velocity using a digital oscilloscope (Wavesurfer, Janelia, VA).

497 Pupil images were acquired at 1280 x 1024 pixels, at 10 Hz from an infrared (IR) camera focused
498 on one eye (Flea3 FL3-U3-13Y3M-C ½" Monochrome USB 3.0 Camera, 1.0x SilverTL Telecentric
499 Lens, FOV = 6.74mm X 5.39mm, Edmund Optics, NJ). The pupil was illuminated by the IR light
500 emitted by the two-photon laser and required no additional IR illumination. Movies were acquired
501 with Matlab Image Acquisition Toolbox (Mathworks, MA). Pupil area was determined in each pupil
502 movie frame post-hoc using custom Matlab code (Mathworks, MA). The pupil was constricted by
503 controlling ambient illumination with an array of LCD screens (LG LP097QX1, South Korea), to
504 maintain a moderate pupil area baseline from which increases and decreases could be
505 measured.

506 *Experimental protocol 3.3*

507 Imaging began 3-5 weeks post-surgery once robust expression of the GCaMP6f virus was
508 observed. Imaging sessions lasted 60-90 min total, divided in half between spontaneous activity
509 and passive listening (ordering was random), and alternated between AC and PPC across days.
510 Fields of view were selected based on co-expression of viral GCaMP6f (all neurons) and
511 transgenic tDTomato (SOM neurons). Multiple imaging sessions were performed in each cranial
512 window, focusing slightly different depths and lateral/posterior locations within the imaging
513 windows across sessions. AC and PPC were each imaged in six mice (biological replicates).
514 Each cranial window was imaged up to 11 times (technical replicates). Imaging from a given

515 cranial window was suspended when we observed nuclear inclusion in 2 or more cells in the field
516 of view, which indicates an over-expression of GCaMP6f. In each imaging session, GCaMP6f
517 fluorescence changes were imaged in SOM (tDTomato+) and Non-SOM neurons, while mice ran
518 freely on a spherical treadmill. In the "spontaneous context", no sensory stimuli were delivered,
519 while in the passive listening context, location-varying sound stimuli were presented.
520 Spontaneous and passive listening contexts lasted ~25-50 minutes each. The order in which the
521 contexts occurred was random.

522 *3.4 Sound stimuli*

523 Either immediately before or following spontaneous activity context, the same field of view was
524 imaged for 25-50 minutes during passive listening. Four magnetic speakers were positioned in a
525 semicircular array, centered on the mouse's head (MF1-S, Tucker-Davis, FL). The speakers were
526 positioned at -90, -30,+30 and +90 degrees in azimuth and driven by digital/analog converter
527 (National Instruments). Speakers were calibrated to deliver similar sound levels (~70 db) in a
528 sound isolation chamber using a microphone at the same distance from the speakers as the
529 mouse's head using a random incidence microphone (4939, Brüel & Kjær, Denmark). During
530 passive listening, 1 or 2 second dynamic ripples (broadband stimuli created in Matlab by
531 summing 32 tones spaced across 2-32 kHz, which fluctuated at 10-20 Hz (87)) were presented
532 from one of eight locations. Four of the sound locations corresponded to the locations of the four
533 speakers (-90, -30, +30, +90 degrees), while the other four sound locations (-60, -15, +15, +60
534 degrees) were simulated using vector based intensity panning, where the same sound stimulus
535 was delivered to two neighboring speakers simultaneously, scaled by a gain factor (45). Dynamic
536 ripples were chosen to optimally drive populations of neurons in auditory cortex with diverse
537 frequency tuning preferences. Each sound repeated three times at one location before switching
538 to another. Each ripple would play from all eight locations in randomized order continuously
539 throughout the session with a 240 ms gap between each sound. Output controlling the audio
540 speakers was aligned with two-photon imaging and running velocity offline using Wavesurfer
541 (Janelia, VA).

542 **4.0 Data Processing**

543 Imaging datasets from 24 AC fields of view and 20 PPC fields of view were included from 6 mice.
544 We excluded any datasets where we observed significant photobleaching or filled cells (see
545 above). We excluded any AC or PPC dataset from analysis if fewer than 1/3 of neurons that were
546 significantly responsive (according to our definition in section 5.1) to at least one sound location,
547 as we were interested in the effect of arousal on both spontaneous and sound-evoked responses.
548 For AC datasets, we analyzed single-cell responses to pure tones on a subset of fields of view
549 from each mouse, and then anatomically aligned all fields of view from datasets collected from
550 each window, to ensure each field of view lay in a region representing tone frequencies in the
551 sonic range of the tonotopic axis of primary auditory cortex. We eliminated any datasets where
552 >50% of tone-responsive neurons had a preferred frequency was in the ultrasonic range
553 (>20kHz), as well as any fields of view that were aligned anterior to a field of view where this was
554 observed, to assure that we were seeing sound responses in the range of frequencies primarily
555 represented by our dynamic ripples (described in section 3.4). We collected widefield
556 fluorescence responses to pure tones in all AC cranial windows and observed ample pure tone
557 responses in the sonic range for all AC windows; however, the extent of the viral expression
558 within windows was too spatially limited to allow for mapping of specific regions.

559 *4.1 Image Processing*

560 For each field of view, the raw calcium movies collected during the spontaneous activity and
561 passive listening contexts were concatenated for motion correction, cell body identification, and
562 fluorescence and neuropil extraction. These processing steps were performed using Suite2p
563 0.9.3 in Python (88). Suite2p first registered images to account for brain motion, and clustered
564 neighboring pixels with similar time courses into regions of interest (ROIs). ROIs were manually
565 curated using the Suite2p GUI, to ensure that only cell bodies as opposed to dendritic processes
566 were included in analysis, based on morphology. Cells expressing tdTomato (SOM cells), were
567 identified using a threshold applied in the Suite2p GUI based on mean fluorescence in the red
568 channel after bleed-through correction applied by Suite2p's cell detection algorithm, along with
569 manual correction. For each ROI, Suite2p returned a raw fluorescence timeseries, as well as an
570 estimate of neuropil fluorescence that could contaminate the signal. For each cell, we scaled the
571 neuropil fluorescence by a factor by 0.7 and subtracted this timeseries from the ROI's raw
572 fluorescence timeseries to obtain a neuropil-corrected fluorescence signal for each selected cell.

573 *4.2 ΔF/F and deconvolution*

574 Once the neuropil corrected fluorescence was obtained for each neuron, we calculated ΔF/F for
575 each cell in each frame by calculating $(F-F_{baseline})/F_{baseline}$ for each frame, where F is the
576 fluorescence of a given cell at that frame and $F_{baseline}$ was the eighth percentile of that cell
577 spanning 450 frames before and after (~15s each way, 30 s total). ΔF/F timeseries were then
578 deconvolved to estimate the relative spike rate in each imaging frame using the OASIS toolbox
579 (89). We used the AR1 FOOPSI algorithm and allowed the toolbox to optimize the convolution
580 kernel, baseline fluorescence, and noise distribution. A threshold of .05 a.u. was applied to
581 remove all events with low magnitude from deconvolved activity timeseries. All analyses were
582 performed with both ΔF/F and deconvolved activity and showed the same trends, unless
583 otherwise indicated. Outside of Figure 1F and 1H only results using deconvolved activity are
584 shown.

585 **5.0 Single cell modulation**

586 *5.1 Sound responsiveness*

587 Sound responsiveness was calculated based on the mean z-scored deconvolved activity of each
588 neuron aligned on sound onset. For each neuron, we calculated the difference between the mean
589 activity during the sound presentation at a certain location (either 1 or 2 seconds) and the mean
590 activity in the 240 milliseconds prior to sound onset. We calculated sound responsiveness
591 separately for each sound location as the mean difference in activity between these two windows
592 for each neuron. We then compared the observed sound responsiveness of each neuron for each
593 sound location to a shuffled distribution. Each cell's activity was shifted randomly by at least 5
594 seconds in time relative to sound location time series, and for 1000 time-shifted iterations, sound
595 responsiveness to each sound location was recalculated. Each sound responsive neuron had a
596 positive sound responsiveness value for at least one location that was greater than the 95th
597 percentile of that cell's shuffled distribution for that location. All other neurons were not
598 considered sound responsive.

599

5.2 Running bouts and modulation

Running bout onsets were defined as transitions in speed from below 10 cm/s to above 10 cm/s, and required that the mean running speed in the 1 s following the transition was three times greater than the 1 s prior to running bout onset, and that the mouse maintained a speed of a minimum of 15 cm/s for the following two seconds.

Running modulation was calculated as the difference in mean z-scored deconvolved activity of a cell in the 1 s prior to running bout onset and the mean activity of a cell in the 3 s window following running bout onset. A shuffling procedure was applied to determine which cells were positively, negatively, and not modulated by running. Each cell's activity was shifted randomly by at least 5 seconds in time relative to running speed timeseries, and for 1000 time-shifted iterations, running modulation was recalculated. Positively modulated neurons had positive running modulation values higher than the 95th percentile of that cell's shuffled distribution. Negatively modulated cells had negative running modulation values lower than the 5th percentile of that cell's shuffled distribution. All other cells were considered to be not modulated by running speed increases.

5.3 Pupil dilation events and modulation

Pupil area was normalized to its maximum across the imaging session. To identify pupil dilation events, we first identified all local maxima of the pupil area. We then found the point prior to this where the derivative of pupil area was zero. We included events where the change from the inflection point to the local maximum was at least a 40% increase in pupil area and that the change from inflection point to local maximum was less than 1 second, and that the local maximum was at least 50% of the maximum total area by the pupil during that imaging session. We considered each inflection point to be the onset of dilation events.

To capture all pupil dilation related activity, which has a slower time course than running (Figure S2), we calculated pupil modulation as the difference between the mean z-scored deconvolved activity in the 1-s time window prior to dilation event onset and the mean activity in the 5-s time window following dilation event onset. We applied the same shuffling procedure described in the section above to determine which neurons were positively, negatively, and not modulated by pupil dilation events.

6.0 Arousal Clustering

6.1 Low and high arousal based on pupil area

K-means clustering was applied to the full pupil area timeseries, which included both spontaneous activity and passive listening contexts, to classify each pupil area value as low, transitional, or high arousal. Each pupil area timeseries was mean normalized using the following equation:

$$\frac{x - \bar{x}}{\bar{x}}$$

The Manhattan (aka City Blocks) distance metric was applied to define 2 centroid clusters that served as the high and low arousal groups. Transition periods included points whose absolute difference in distance to the high and low arousal centroids was less than 0.05.

6.2 Arousal Modulation Index

Arousal modulation index was calculated for each neuron using the following equation:

$$\frac{FR_{hi} - FR_{lo}}{FR_{hi} + FR_{lo}}$$

For FR, we first maximum-normalized the deconvolved activity trace of each neuron. For FR_{hi}, we summed the maximum-normalized deconvolved activity during frames in the "high" cluster and divided that by the total time spent in the high cluster during either the spontaneous (Figure 2) or passive (Figure S3). FR_{lo} was determined similarly, using the low arousal cluster. This index allowed a modulation index between -1 and 1, where negative values indicated higher activity in the low arousal cluster, and positive numbers indicated higher activity during the high arousal cluster.

7.0 Noise Correlations

Pairwise Correlations 7.1

Pairwise noise correlations were calculated based on trial-to-trial fluctuations around mean sound-evoked responses. One sound trial included three repeats of a given sound stimulus. We calculated mean sensory-evoked activity for each neuron at each location and binned the activity of each neuron by 10 frames (~330 milliseconds) over the course of the sound trial. Trials were either 3 or 6 seconds long depending on the duration of the dynamic ripple. Mean responses were calculated separately for different durations at the same location. For each neuron, we subtracted the mean sensory response for each location at each trial, and then concatenated these mean-subtracted trial responses. For each pair of neurons, we computed the Pearson correlation coefficient between these binned, mean-subtracted activity timeseries. We also calculated a shuffled distribution of pairwise noise correlations by shuffling the identity of trials for each neuron independently within sound location/duration condition and then computing the Pearson correlation coefficient in the same way. We also computed signal correlation between each pair of neurons, as the Pearson correlation between the pair of neurons' mean sound-evoked responses to each sound duration/location after they had been binned into 10 frame (~330 milliseconds) bins and concatenated.

During the spontaneous context, a similar approach was used to find running-based noise correlations. The three seconds following each running bout onset was defined as a "trial", and the Pearson correlation was computed based on the binned (~330 ms) activity of pairs of neurons after subtracting mean running-related activity from each neuron's timeseries.

7.2 Noise correlations in low and high arousal clusters

Because it was rare for a mouse's pupil to remain in either the high or low arousal cluster for the entire 3-6 s duration of a trial based on all three repetitions of a sound location, we instead focused this analysis on first of the three sound stimulus repeats within a trial. We defined a sound trial as "high arousal" if 90% of imaging frames collected during that sound presentation were classified within the high arousal cluster (Materials and Methods 6.1), and as "low arousal" if 90% of imaging frames collected during that sound presentation were classified within the low arousal cluster. As before, we binned each neuron's activity in 10 frame (330 ms) bins. For each

trial classified as high or low arousal, each cell's the mean sound response to all matching sound location/duration first repetition presentations (including trials belonging to low, high, or neither cluster) was subtracted. Because the ratio of low and high arousal trials was different across days for different mice, we balanced the number of sound location trials by a sub-sampling procedure, where for 10 iterations a random subset of trials was selected from the arousal cluster that had more trials to match the number of trials of the rarer arousal cluster. We only included data from sessions where there were at least 100 first-repeat trials balanced for sound location and duration in both the high and low arousal cluster, and where there were at least 5 trials representing each sound location in both low and high arousal. Within each arousal cluster (low and high), the Pearson correlation was computed for each pair of neurons' sub-sampled, mean-subtracted activity traces.

7.3 Correlation decay over distance

We considered pairs of neurons in four separate distance bins, pairs of neurons within 0-100, 100-200, 200-300, 300+μm from each other. For all neuron pairs, as well as by dataset, we fit decay constant λ based on the mean noise correlations of pairs in each bin using the following equation:

$$\frac{\delta\rho}{\delta\mu m} = -\lambda\mu m$$

Where ρ is the pairwise noise correlation between cells, and l is a decay constant that describes the rate of decay over distance (μm). We calculated this decay constant, l, using noise correlations based on trial-to-trial fluctuations centered either on mean sound-location related responses during the passive listening context (Figure 5G), or on mean running bout related responses during the spontaneous context (Figure S8D). This decay constant, l, was calculated considering the means of each distance bin using all pairs from all datasets, as well as for each dataset considered separately.

8.0 Encoding Models

Using Generalized Linear Models (GLMs), the time-dependent effects of all measured external variables and activity of neighboring neurons on each neuron's activity were estimated (45, 46). For this approach, several classes of predictors were used in different combinations: running, pupil, sound location, and activity of SOM or Non-SOM neurons. We used a Bernoulli-based GLM to weight various combinations of predictors based on these variables to predict each neuron's binarized activity (timeseries of relative spike rates were thresholded at 0.05). The encoding model is fully described in our previous work (45)

8.1 Pupil and Running Predictors

Running velocity was measured at a higher time resolution than imaging and was binned to match the sampling rate of two-photon images (30 Hz). We included the velocity along the pitch and roll axes of the treadmill (relative to the mouse's body axis). Running velocity measurements were separated into four channels, (1) forward, (2) reverse, (3) left, (4) right directions based on rotation along these axes. Running velocity changes could both precede or follow activity of individual neurons, so time series of running velocity were convolved with four evenly spaced Gaussian basis functions (240 milliseconds half-width at half-height) extending 1s both forward

and backward in time (8 basis functions total for each running direction: forward, reverse, left, and right, Figure S6). Changes in pupil area were modeled similarly. Because pupil is a slower signal, the pupil area trace was convolved with 16 evenly spaced Gaussian basis functions 4s forward and backward in time to allow either prediction or response to pupil area changes.

8.2 Sound Stimulus Predictors

For sound stimulus onsets at each of the possible sound locations, 12 evenly spaced Gaussian basis functions (170 millisecond half width at half height) extended 2 s forward in time from each sound onset. First, second, and third repeats were represented separately due to potential adaptation-related effects. This resulted in 12 basis functions per repeat per sound location x 3 repeats x 8 locations for 288 sound predictors.

8.3 Coupling Predictors

For a given neuron being fitted, the relative spike rate of all individual SOM neurons as well as their activity averaged across cells was convolved with two boxcar functions extending ~66 milliseconds forward in time from the activity of the predictor neurons (each boxcar was non-zero for only a single imaging frame or ~33 milliseconds). Because in all datasets there were more Non-SOM neurons than SOM neurons, to estimate Non-SOM coupling, a separate set of Non-SOM predictors was randomly selected for each neuron to match the population size and distance of the SOM neurons from that neuron. Creating these separate sets of predictors allowed us to compare functional coupling within and between the SOM and Non-SOM populations within each field of view.

8.4 GLM fitting procedure

All predictors were maximum normalized before the fitting procedure. Beta coefficients for the predictors were fitted to each neuron's activity individually, using the glmnet package in R (90) with elastic-net regularization, which smoothly interpolated between L_1 and L_2 type regularization according to the value of an interpolation parameter α, such that α=0 corresponded to L_2 and α=1 corresponded to L_1. We selected α=.25.

The GLMs were fit separately for the spontaneous and passive listening contexts. Within each context, trials were randomly split into training (70% of trials) and test (remaining 30% of trials) sets, while balancing the distribution of sound locations. Fitting was performed on the training set, and within each training dataset, cross validation folds (3x) were also pre-selected so that sound locations were evenly represented. Model performance (see below, 8.5) was assessed on the test set. Each model was thus fitted and tested on entirely separate data to prevent over-fitting concerns. This train/test procedure was repeated ten times, with random subsamples of the data included in train and test segments. Each model's overall performance was assessed as its mean across all 10 iterations.

8.5 GLM model performance

Each model's performance for each cell was defined as the fraction of explained deviance of each model (compared to the null model). In the null model, only a constant (single parameter) was used to fit the neuron's activity and no time-varying predictors were included. We calculated the deviance of the null and behavior and coupling model variants. For each model, the fraction of

null model deviance explained by the model was then calculated ((null deviance – model deviance)/null deviance). Deviance calculations were performed on a test dataset (30% of the data), which had not been included in the fitting procedure, and this train/test procedure was repeated ten times on randomly subsampled segments of the data.

8.6 Running and pupil contribution

While running and pupil area fluctuations are highly correlated, they have separable influences on neural activity (6). To identify the separate contributions of running and pupil area on SOM and Non-SOM neurons, we fit three separate models: (1) full behavior model, (2) “no pupil” model, (3) “no running” model. In the full behavior model, all running, pupil, and sound predictors were included to fit each neuron’s activity. The “no pupil” model did not include the pupil predictors, and the “no running model” did not include the running predictors.

By comparing the model performance (fraction deviance explained, see above 8.5) in the full vs. no pupil or no running models, we estimated the contribution of pupil or running to a neuron’s activity, that could not be compensated for by the other variable. Running contribution was calculated as the difference in fraction deviance explained of the full model and fraction deviance explained of the no-running model d_{fb}-d_{nr}. Pupil contribution was calculated as the difference in fraction deviance explained of the full model and fraction deviance explained of the no-pupil model d_{fb}-d_{np}.

8.7 Coupling

We previously demonstrated that by comparing the model performance (fraction of explained deviance) in the coupled model to the performance of the uncoupled model, we could estimate the level of correlation between a given neuron and the neurons in the simultaneously imaged population, while considering the contributions of behavior and stimulus-related variables (45).

Here, we computed several types of “coupling” by comparing the model performance (fraction deviance explained) of each coupled variant of the model to the behavior-only model. We computed three types of coupling: (1) Non-SOM/Non-SOM coupling, (2) SOM/SOM coupling, (3) Non-SOM/SOM coupling. Each type of coupling was computed in the same way, as the difference between the fraction deviance explained of the full behavior model and the fraction deviance explained of a coupled model using other neurons as predictors. However, for each type of coupling, there was a different combination of the type of cell being fit and the type of predictors being used to fit that cell, as follows:

1) Non-SOM/Non-SOM coupling: Defined as the improvement in model performance when using Non-SOM predictors to explain Non-SOM activity, compared to the behavior-only model, $d_{Non\text{-}SOM}$-d_{behav}
2) SOM/SOM coupling: Defined as the improvement in model performance when using other SOM predictors to explain SOM activity, compared to the behavior-only model, d_{SOM}-d_{behav}
3) Non-SOM/SOM coupling: Defined as the improvement in model performance when using Non-SOM predictors to explain SOM activity, compared to the behavior only model, $d_{Non\text{-}SOM}$-d_{behav}.

These various types of coupling allow a characterization of the functional relationships among distinct classes of neurons across cortical areas.

9.0 Decoding

The details of the decoder that we built to estimate the information in AC and PPC populations about sound stimulus have been previously described (45). Briefly, for each trial we decoded sound stimulus location from single-trial population activity by computing the probability of external variables (sound location Left/Right category, or specific sound location) given population activity. We used Bayes' theorem and population response probabilities estimated through the behavior-only (uncoupled) GLM and its predictors in that trial to compute the posterior probability of each possible sound location stimulus. The decoder was "cumulative" in time, as for each time point t, it was based on all imaging frames from the initiation of the trial time t. The decoded stimulus location at each time t was defined as the stimulus location with the maximum posterior probability, based on individual neurons or on a population of simultaneously imaged neurons. The population could include SOM, Non-SOM, or the "best" neurons. Non-SOM neurons were randomly subsampled 10 times, matching the sample size of SOM neurons in each iteration. The "best" neurons were selected as the n individual neurons with the best decoding performance, where n is the number of SOM neurons simultaneously imaged. Decoder performance was calculated as the fraction of correctly classified trials at each time point.

To compare decoder performance in low and high arousal states, trials were classified as "low" or "high" arousal based on normalized pupil area (see section 7.2). Only the first sound repeat of each trial was used. Trials were randomly subsampled in the test set to ensure an even distribution of low and high arousal trials, and sound locations. This random subsample was repeated ten times.

10.0 Sound location selectivity

To assess the selectivity of sound-related activity in SOM and Non-SOM neurons in AC and PPC, trial-averaged responses were used to calculate the "location selectivity index", based on vector averaging in the preferred sound direction:

$$LSI = \sqrt{\left(\sum_{i=1}^{n} R(\Theta_i)cos(2\Theta_i)^{2} + \sum_{i=1}^{n} R(\Theta_i)sin(2\Theta_i)^{2}\right)} / \sum_{i=1}^{n} R_i$$

where R is the average response during the sound location presentation, and Θ is the sound location from -90 to +90 degrees, indexed by I = 1 to n (8). LSI can vary continuously from 0 (unselective) to 1 (selectively responding to only one sound location).

11.0 Histology

After all imaging sessions had been acquired, each mouse was transcardially perfused with saline and then 4% paraformaldehyde. The brain was extracted, cryoprotected, embedded, frozen, and sliced. Once slide mounted, we stained brains with DAPI to be able to identify structure. We used anatomical structure to verify the locations of our injections in AC and PPC.

Acknowledgments
We thank Chengcheng Huang, Ross Williamson, and members of the Runyan lab for comments on the manuscript. This research was supported in part by the University of Pittsburgh Center for Research Computing through the resources provided. Judith Joyce Balcita-Pedicino performed histology and immunohistochemistry. We thank the GENIE project (Janelia) for making GCaMP sensors available for use. We thank the developers of Suite2P and Wavesurfer. This work was supported by the Andrew W. Mellon Predoctoral Fellowship, NIH Predoctoral Training Grant in Basic Neuroscience (T32 NS007433-21), Pew Biomedical Scholars Program, the Searle Scholars Program, the Klingenstein-Simons Fellowship Award in Neuroscience, and NIH grants NIMH DP2MH122404, NINDS R01NS121913.

References

1. M. R. Cohen, J. H. R. Maunsell, Attention improves performance primarily by reducing interneuronal correlations. *Nature Neuroscience* 12, 1594–1600 (2009).

2. N. C. Rabinowitz, R. L. Goris, M. Cohen, E. P. Simoncelli, Attention stabilizes the shared gain of V4 populations. *eLife* 4, e08998 (2015).

3. C. J. McAdams, J. H. Maunsell, Effects of attention on orientation-tuning functions of single neurons in macaque cortical area V4. *J Neurosci Official J Soc Neurosci* 19, 431–41 (1999).

4. S. Treue, J. H. R. Maunsell, Attentional modulation of visual motion processing in cortical areas MT and MST. *Nature* 382, 539–541 (1996).

5. J. F. Mitchell, K. A. Sundberg, J. H. Reynolds, Spatial Attention Decorrelates Intrinsic Activity Fluctuations in Macaque Area V4. *Neuron* 63, 879–888 (2009).

6. M. Vinck, R. Batista-Brito, U. Knoblich, J. A. Cardin, Arousal and Locomotion Make Distinct Contributions to Cortical Activity Patterns and Visual Encoding. *Neuron* 86, 740–754 (2015).

7. J. F. A. Poulet, C. C. H. Petersen, Internal brain state regulates membrane potential synchrony in barrel cortex of behaving mice. *Nature* 454, 881–885 (2008).

8. M. Zhou, *et al.*, Scaling down of balanced excitation and inhibition by active behavioral states in auditory cortex. *Nature Neuroscience* 17, 841–850 (2014).

9. P.-A. Lin, S. K. Asinof, N. J. Edwards, J. S. Isaacson, Arousal regulates frequency tuning in primary auditory cortex. *Proc National Acad Sci* 116, 25304–25310 (2019).

10. C. M. Niell, M. P. Stryker, Modulation of Visual Responses by Behavioral State in Mouse Visual Cortex. *Neuron* 65, 472–479 (2010).

11. Y. Fu, *et al.*, A Cortical Circuit for Gain Control by Behavioral State. *Cell* 156, 1139–1152 (2014).

12. P. J. Mineault, E. Tring, J. T. Trachtenberg, D. L. Ringach, Enhanced Spatial Resolution During Locomotion and Heightened Attention in Mouse Primary Visual Cortex. *The Journal of neuroscience : the official journal of the Society for Neuroscience* 36, 6382–6392 (2016).

13. P.-O. Polack, J. Friedman, P. Golshani, Cellular mechanisms of brain state–dependent gain modulation in visual cortex. *Nat Neurosci* 16, 1331–1339 (2013).

14. M. J. McGinley, S. V. David, D. A. McCormick, Cortical Membrane Potential Signature of Optimal States for Sensory Signal Detection. *Neuron* 87, 179–192 (2015).

15. C. Bennett, S. Arroyo, S. Hestrin, Subthreshold Mechanisms Underlying State-Dependent Modulation of Visual Responses. *Neuron* 80, 350–357 (2013).

16. D. Shimaoka, K. D. Harris, M. Carandini, Effects of Arousal on Mouse Sensory Cortex Depend on Modality. *Cell Reports* 25, 3230 (2018).

17. D. M. Schneider, A. Nelson, R. Mooney, A synaptic and circuit basis for corollary discharge in the auditory cortex. *Nature* 513, 189–194 (2014).

18. I. Yavorska, M. Wehr, Effects of Locomotion in Auditory Cortex Are Not Mediated by the VIP Network. *Front Neural Circuit* 15, 618881 (2021).

19. R. Tremblay, S. Lee, B. Rudy, GABAergic Interneurons in the Neocortex: From Cellular Properties to Circuits. *Neuron* 91, 260–292 (2016).

20. E. E. Fanselow, K. A. Richardson, B. W. Connors, Selective, state-dependent activation of somatostatin-expressing inhibitory interneurons in mouse neocortex. *Journal of neurophysiology* 100, 2640–2652 (2008).

21. M. Beierlein, J. R. Gibson, B. W. Connors, A network of electrically coupled interneurons drives synchronized inhibition in neocortex. *Nat Neurosci* 3, 904–910 (2000).

22. N. Chen, H. Sugihara, M. Sur, An acetylcholine-activated microcircuit drives temporal dynamics of cortical activity. *Nature Neuroscience* 18, 892–902 (2015).

23. Z. Xiang, J. R. Huguenard, D. A. Prince, Cholinergic switching within neocortical inhibitory networks. *Science* 281, 985–988 (1998).

24. Y. Kawaguchi, T. Shindou, Noradrenergic Excitation and Inhibition of GABAergic Cell Types in Rat Frontal Cortex. *J Neurosci* 18, 6963–6976 (1998).

25. K. V. Kuchibhotla, *et al.*, Parallel processing by cortical inhibition enables context-dependent behavior. *Nature Neuroscience* (2016) https:/doi.org/10.1038/nn.4436.

26. C. K. Pfeffer, M. Xue, M. He, Z. J. Huang, M. Scanziani, Inhibition of Inhibition in Visual Cortex: The Logic of Connections Between Molecularly Distinct Interneurons. *Nat Neurosci* 16, 1068–1076 (2013).

27. M. Dipoppa, *et al.*, Vision and Locomotion Shape the Interactions between Neuron Types in Mouse Visual Cortex. *Neuron* 98, 602-615.e8 (2018).

28. P. Garcia-Junco-Clemente, *et al.*, An inhibitory pull-push circuit in frontal cortex. *Nat Neurosci* 20, 389–392 (2017).

29. H.-J. Pi, *et al.*, Cortical interneurons that specialize in disinhibitory control. *Nature* 503, 521–524 (2013).

30. M. M. Karnani, *et al.*, Opening Holes in the Blanket of Inhibition: Localized Lateral Disinhibition by VIP Interneurons. *J Neurosci* 36, 3471–3480 (2016).

31. E. Fino, R. Yuste, Dense Inhibitory Connectivity in Neocortex. *Neuron* 69, 1188–1203 (2011).

32. H. Xu, H.-Y. Jeong, R. Tremblay, B. Rudy, Neocortical Somatostatin-Expressing GABAergic Interneurons Disinhibit the Thalamorecipient Layer 4. *Neuron* 77, 155–167 (2013).

33. H. Adesnik, W. Bruns, H. Taniguchi, Z. J. Huang, M. Scanziani, A neural circuit for spatial summation in visual cortex. *Nature* 490, 226–231 (2012).

34. N. R. Wilson, C. A. Runyan, F. L. Wang, M. Sur, Division and subtraction by distinct cortical inhibitory networks in vivo. *Nature* 488, 343–348 (2012).

35. R. V. Rikhye, M. Yildirim, M. Hu, V. Breton-Provencher, M. Sur, Reliable sensory processing in mouse visual cortex through cooperative interactions between somatostatin and parvalbumin interneurons. *J Neurosci*, JN-RM-3176-20 (2021).

36. J. Veit, R. Hakim, M. P. Jadi, T. J. Sejnowski, H. Adesnik, Cortical gamma band synchronization through somatostatin interneurons. *Nature Neuroscience* 20, 951–959 (2017).

37. H. K. Kato, S. N. Gillet, J. S. Isaacson, Flexible Sensory Representations in Auditory Cortex Driven by Behavioral Relevance. *Neuron* 88, 1027–1039 (2015).

38. X.-J. Wang, G. R. Yang, A disinhibitory circuit motif and flexible information routing in the brain. *Curr Opin Neurobiol* 49, 75–83 (2018).

39. Y. Kim, *et al.*, Brain-wide Maps Reveal Stereotyped Cell-Type-Based Cortical Architecture and Subcortical Sexual Dimorphism. *Cell* 171, 456-469.e22 (2017).

40. S. J. Dienel, *et al.*, Distinct Laminar and Cellular Patterns of GABA Neuron Transcript Expression in Monkey Prefrontal and Visual Cortices. *Cereb Cortex* 31, bhaa341- (2020).

41. H. Taniguchi, *et al.*, A resource of Cre driver lines for genetic targeting of GABAergic neurons in cerebral cortex. *Neuron* 71, 995–1013 (2011).

42. L. Madisen, *et al.*, A robust and high-throughput Cre reporting and characterization system for the whole mouse brain. *Nature Neuroscience* 13, 133–140 (2009).

43. T.-W. Chen, *et al.*, Ultrasensitive fluorescent proteins for imaging neuronal activity. *Nature* 499, 295–300 (2013).

44. K. Nakamura, Auditory spatial discriminatory and mnemonic neurons in rat posterior parietal cortex. *Journal of neurophysiology* 82, 2503–2517 (1999).

45. C. A. Runyan, E. Piasini, S. Panzeri, C. D. Harvey, Distinct timescales of population coding across cortex. *Nature* 548, 92–96 (2017).

46. J. W. Pillow, *et al.*, Spatio-temporal correlations and visual signalling in a complete neuronal population. *Nature* 454, 995–999 (2008).

47. I. M. Park, M. L. R. Meister, A. C. Huk, J. W. Pillow, Encoding and decoding in parietal cortex during sensorimotor decision-making. *Nature Neuroscience* 17, 1395–1403 (2014).

48. M. Minderer, K. D. Brown, C. D. Harvey, The Spatial Structure of Neural Encoding in Mouse Posterior Cortex during Navigation. *Neuron* (2019) https:/doi.org/10.1016/j.neuron.2019.01.029.

49. D. A. Nitz, Tracking route progression in the posterior parietal cortex. *Neuron* 49, 747–756 (2006).

50. J. R. Whitlock, G. Pfuhl, N. Dagslott, M.-B. Moser, E. I. Moser, Functional split between parietal and entorhinal cortices in the rat. *Neuron* 73, 789–802 (2012).

51. M. Krumin, J. J. Lee, K. D. Harris, M. Carandini, Decision and navigation in mouse parietal cortex. *Elife* 7, e42583 (2018).

52. C. D. Harvey, P. Coen, D. W. Tank, Choice-specific sequences in parietal cortex during a virtual-navigation decision task. *Nature* 484, 62–68 (2012).

53. A. M. Licata, *et al.*, Posterior Parietal Cortex Guides Visual Decisions in Rats. *J Neurosci* 37, 4954–4966 (2017).

54. G. H. Otazu, L.-H. Tai, Y. Yang, A. M. Zador, Engaging in an auditory task suppresses responses in auditory cortex. *Nature Neuroscience* 12, 646–654 (2009).

55. J. Fritz, S. Shamma, M. Elhilali, D. Klein, Rapid task-related plasticity of spectrotemporal receptive fields in primary auditory cortex. *Nat Neurosci* 6, 1216–1223 (2003).

56. D. Saderi, Z. P. Schwartz, C. R. Heller, J. R. Pennington, S. V. David, Dissociation of task engagement and arousal effects in auditory cortex and midbrain. *Elife* 10, e60153 (2021).

57. M. J. Goard, G. N. Pho, J. Woodson, M. Sur, Distinct roles of visual, parietal, and frontal motor cortices in memory-guided sensorimotor decisions. *eLife* (2016).

58. G. N. Pho, M. J. Goard, J. Woodson, B. Crawford, M. Sur, Task-dependent representations of stimulus and choice in mouse parietal cortex. *Nat Commun* 9, 2596 (2018).

59. A. M. Packer, R. Yuste, Dense, unspecific connectivity of neocortical parvalbumin-positive interneurons: a canonical microcircuit for inhibition? *The Journal of neuroscience : the official journal of the Society for Neuroscience* 31, 13260–13271 (2011).

60. S. B. Hofer, *et al.*, Differential connectivity and response dynamics of excitatory and inhibitory neurons in visual cortex. *Nature Neuroscience* 14, 1045–1052 (2011).

61. H. Ko, *et al.*, Functional specificity of local synaptic connections in neocortical networks. *Nature* 473, 87–91 (2011).

62. Y. Yoshimura, J. L. M. Dantzker, E. M. Callaway, Excitatory cortical neurons form fine-scale functional networks. *Nature* 433, 868–873 (2005).

63. Y. Yoshimura, E. M. Callaway, Fine-scale specificity of cortical networks depends on inhibitory cell type and connectivity. *Nature Neuroscience* 8, 1552–1559 (2005).

64. D. V. Buonomano, W. Maass, State-dependent computations: spatiotemporal processing in cortical networks. *Nature Reviews Neuroscience* 10, 113–125 (2009).

65. C. Huang, *et al.*, Circuit Models of Low-Dimensional Shared Variability in Cortical Networks. *Neuron* 101, 337-348.e4 (2019).

66. M. Valente, *et al.*, Correlations enhance the behavioral readout of neural population activity in association cortex. *Nat Neurosci* 24, 975–986 (2021).

67. M. M. Karnani, *et al.*, Cooperative Subnetworks of Molecularly Similar Interneurons in Mouse Neocortex. *Neuron* 90, 86–100 (2016).

68. R. A. Andersen, C. A. Buneo, INTENTIONAL MAPS IN POSTERIOR PARIETAL CORTEX. *Annu Rev Neurosci* 25, 189–220 (2002).

69. L. Waschke, S. Tune, J. Obleser, Local cortical desynchronization and pupil-linked arousal differentially shape brain states for optimal sensory performance. *Elife* 8, e51501 (2019).

70. J. Urban-Ciecko, A. L. Barth, Somatostatin-expressing neurons in cortical networks. *Nat Rev Neurosci* 17, 401–409 (2016).

71. J. M. Pakan, *et al.*, Behavioral-state modulation of inhibition is context-dependent and cell type specific in mouse visual cortex. *Elife* 5, e14985 (2016).

72. S. Lee, I. Kruglikov, Z. J. Huang, G. Fishell, B. Rudy, A disinhibitory circuit mediates motor integration in the somatosensory cortex. *Nature Neuroscience* 16, 1662–1670 (2013).

73. S. Musall, M. T. Kaufman, A. L. Juavinett, S. Gluf, A. K. Churchland, Single-trial neural dynamics are dominated by richly varied movements. *Nat Neurosci* 22, 1677–1686 (2019).

74. C. Stringer, *et al.*, Spontaneous behaviors drive multidimensional, brainwide activity. *Science* 364, eaav7893 (2019).

75. U. Knoblich, L. Huang, H. Zeng, L. Li, Neuronal cell-subtype specificity of neural synchronization in mouse primary visual cortex. *Nat Commun* 10, 2533 (2019).

76. A. G. Khan, *et al.*, Distinct learning-induced changes in stimulus selectivity and interactions of GABAergic interneuron classes in visual cortex. *Nature Neuroscience* 21, 851–859 (2018).

77. G. Rothschild, I. Nelken, A. Mizrahi, Functional organization and population dynamics in the mouse primary auditory cortex. *Nat Neurosci* 13, 353–360 (2010).

78. R. Rosenbaum, M. A. Smith, A. Kohn, J. E. Rubin, B. Doiron, The spatial structure of correlated neuronal variability. *Nat Neurosci* 20, 107–114 (2017).

79. M. A. Smith, A. Kohn, Spatial and Temporal Scales of Neuronal Correlation in Primary Visual Cortex. *The Journal of neuroscience : the official journal of the Society for Neuroscience* 28, 12591–12603 (2008).

80. M. I. Chelaru, V. Dragoi, Negative Correlations in Visual Cortical Networks. *Cereb Cortex* 26, 246–256 (2016).

81. D. P. A. Schulz, M. Sahani, M. Carandini, Five key factors determining pairwise correlations in visual cortex. *J Neurophysiol* 114, 1022–1033 (2015).

82. M. A. Smith, M. A. Sommer, Spatial and Temporal Scales of Neuronal Correlation in Visual Area V4. *J Neurosci* 33, 5422–5432 (2013).

83. S. Safavi, *et al.*, Nonmonotonic spatial structure of interneuronal correlations in prefrontal microcircuits. *Proc National Acad Sci* 115, 201802356 (2018).

84. H. K. Kato, S. K. Asinof, J. S. Isaacson, Network-Level Control of Frequency Tuning in Auditory Cortex. *Neuron* 95, 412-423.e4 (2017).

85. A. C. Huk, M. N. Shadlen, Neural activity in macaque parietal cortex reflects temporal integration of visual motion signals during perceptual decision making. *The Journal of neuroscience : the official journal of the Society for Neuroscience* 25, 10420–10436 (2005).

86. J. K. Fitzgerald, D. J. Freedman, J. A. Assad, Generalized associative representations in parietal cortex. *Nature Neuroscience* 14, 1075–1079 (2011).

87. M. Elhilali, J. B. Fritz, D. J. Klein, J. Z. Simon, S. A. Shamma, Dynamics of precise spike timing in primary auditory cortex. *The Journal of neuroscience : the official journal of the Society for Neuroscience* 24, 1159–1172 (2004).

88. M. Pachitariu, *et al.*, Suite2p: beyond 10,000 neurons with standard two-photon microscopy. *Biorxiv*, 061507 (2017).

89. J. Friedrich, P. Zhou, L. Paninski, Fast online deconvolution of calcium imaging data. *Plos Comput Biol* 13, e1005423 (2017).

90. J. Friedman, T. Hastie, R. Tibshirani, Regularization Paths for Generalized Linear Models via Coordinate Descent. *Journal of Statistical Software* 33 (2010).

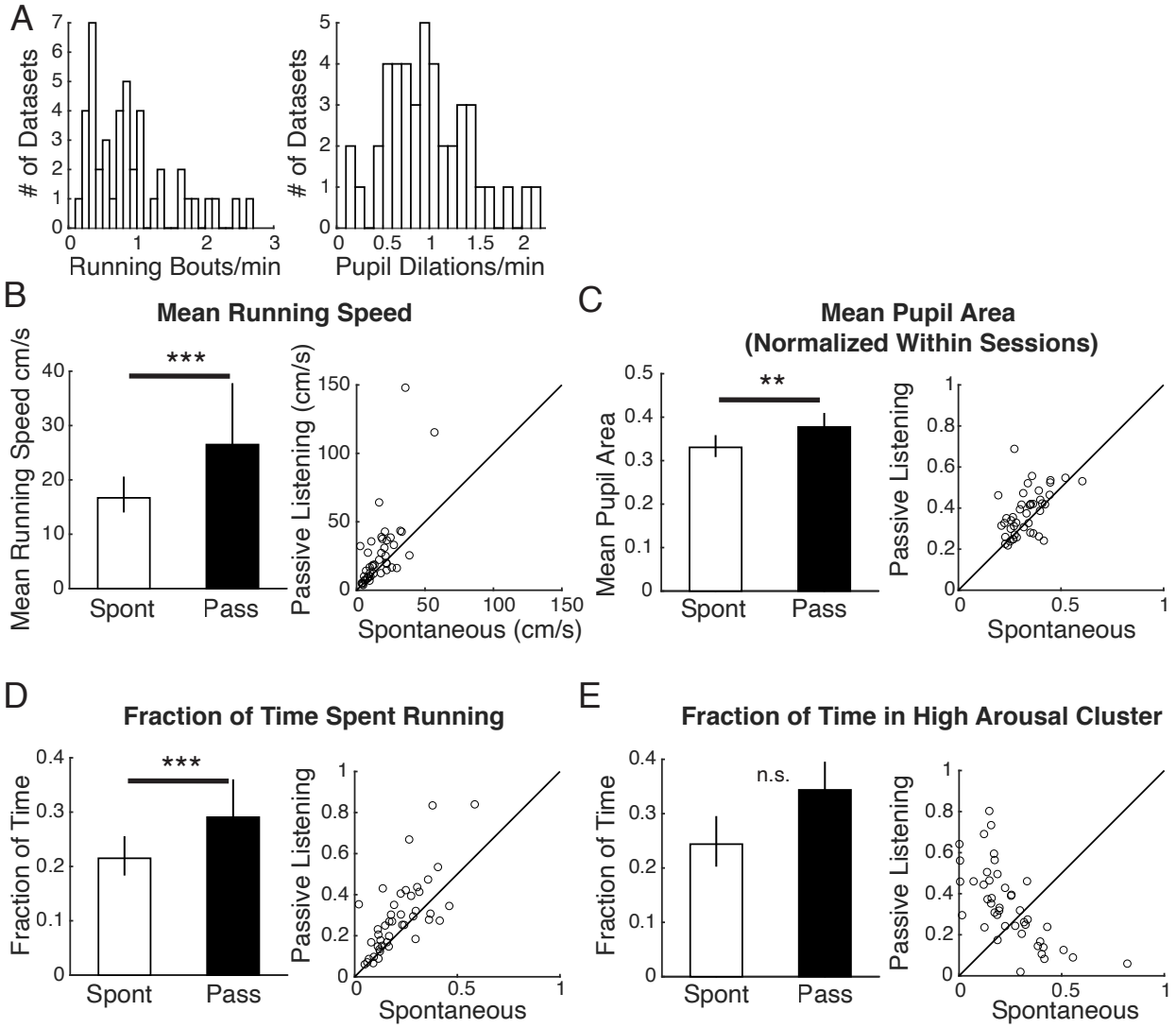

Figure S1: Running behavior and pupil area across imaging sessions. (A) Overall frequency of behavioral state changes, quantified as running bouts (left) and pupil dilations (right), as defined in Materials and Methods; N=44 datasets. (B) Left: Mean running speed in the spontaneous and passive listening behavioral contexts. Right: Mean running speed during the passive listening context plotted against the mean running speed during the spontaneous context, for each imaging session. (C) As in B, for pupil area (normalized across each session). (D) Left: Mean fraction of time spent running in spontaneous and passive listening behavioral contexts. Right: Fraction of time spent running during the passive listening context plotted against the fraction of time spent running during the spontaneous context. (E) As in D, but for time spent in the "high arousal cluster", see Materials and Methods. ***p<0.001; **p<.01; n.s. not significant. Error bars indicate bootstrapped 95% confidence intervals. See Table S1 for related statistics.

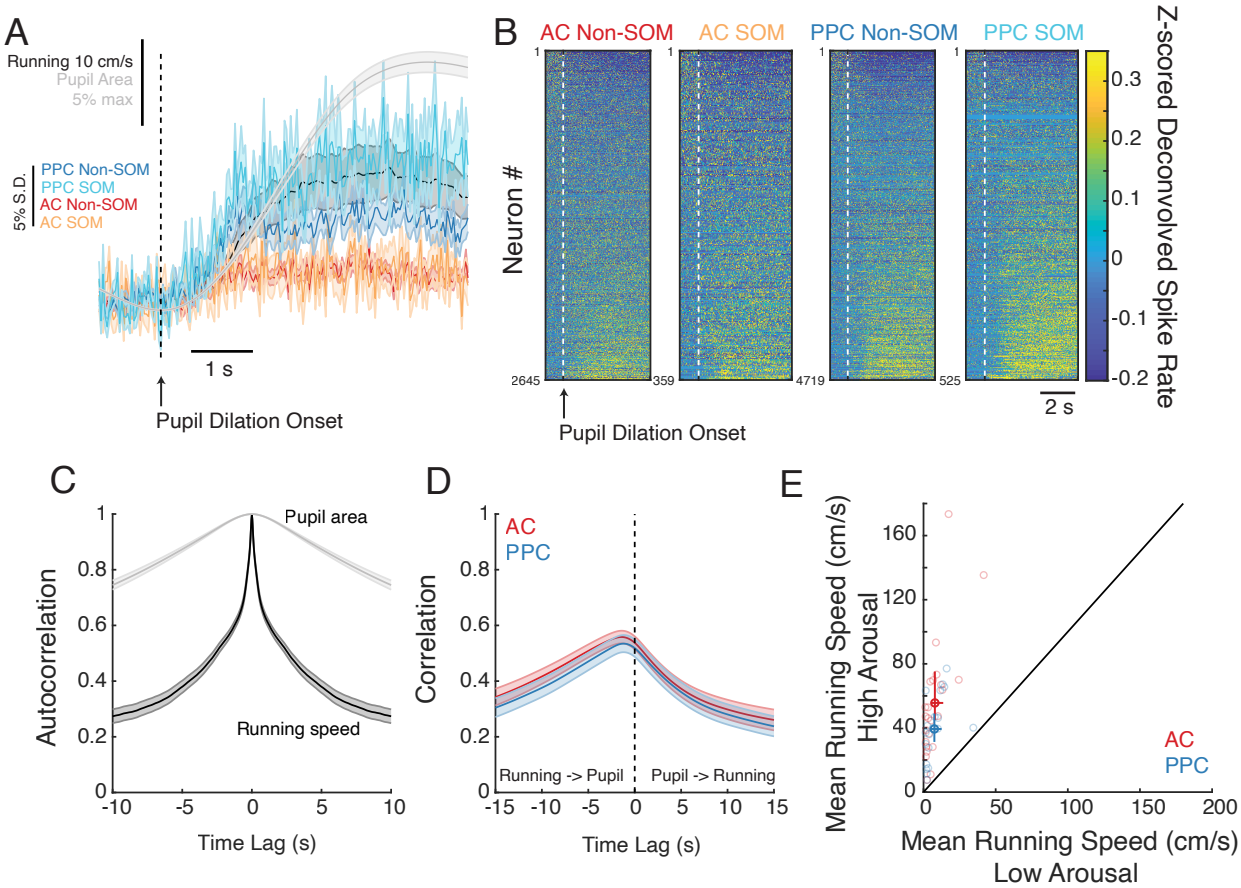

Figure S2: Pupil dilation events, and the relationship between pupil area and running speed. (A) Running speed, pupil area, and single neuron activity, aligned and averaged on pupil dilation events (as compared to running bouts of Figure 3A), N=44 datasets. (B) Average activity, z-scored deconvolved spike rates, of all AC Non-SOM (N=2645), AC SOM (N=359), PPC Non-SOM (N=4719), and PPC SOM (N=525) neurons, aligned on pupil dilation events. Neurons were sorted by pupil modulation. (C) Autocorrelation of pupil area and running speed, averaged across all datasets (N=44). (D) Crosscorrelation between running speed and pupil area, averaged across AC datasets (red, N=24) and PPC datasets (blue, N=20). (E) Mean running speed in high arousal states (defined as dilated pupil cluster, as in Figure 2) plotted against mean running speed in low arousal states, for individual AC and PPC datasets (light), and averaged across datasets (bold). Shading indicates SEM.

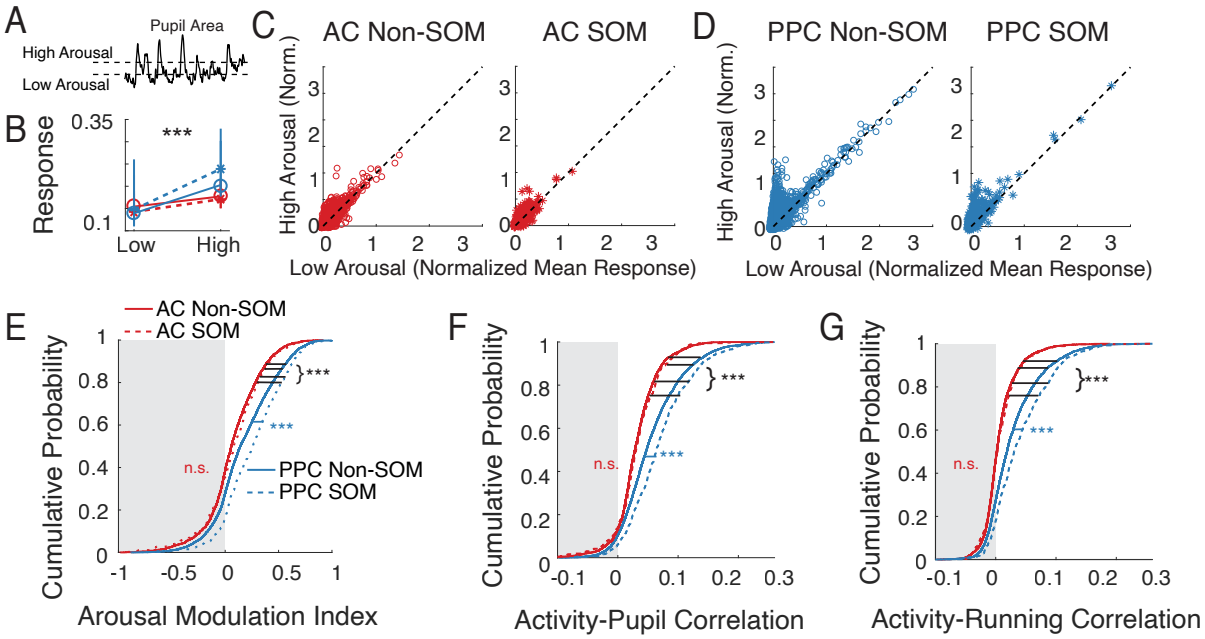

Figure S3: Single cell activity relationships with pupil area and running speed, in the passive listening context. Analyses are the same as presented in Figure 2C-I, but in the passive listening context. AC Non-SOM N=2645; AC SOM N=359; PPC Non-SOM N=4719; PPC SOM N=525 for all panels. (A) Example of clustering that sorted pupil area during each imaging frame into low, transition, and high arousal states. (B) Mean responses of AC Non-SOM (red solid), AC SOM (red dotted), PPC Non-SOM (blue solid), and PPC SOM (blue dotted) neurons in low and high arousal states, as defined in A. ***p<.001, lines represent bootstrapped 95% confidence intervals. (C) Left: Mean activity of AC Non-SOM neurons in high arousal state (classified with clustering as in A), plotted against mean activity in the low arousal state. Right: Mean activity of AC SOM neurons in high arousal vs low arousal states. (D) As in C, for PPC Non-SOM and SOM neurons. (E) Cumulative probability distribution of the arousal modulation index in AC Non-SOM (solid red), AC SOM (dotted red), PPC Non-SOM (solid blue), and PPC SOM (dotted blue) neurons. Arousal modulation index was calculated from the values in C-D, (High-Low)/(High+Low) for each neuron. (F) Cumulative probability distribution of the Pearson correlation between each neuron's activity and pupil area, colors as in E. (G) Cumulative probability distribution of the Pearson correlation between each neuron's activity and running speed. Full summary of statistics an dvalues a vailable in Tables S4-5.

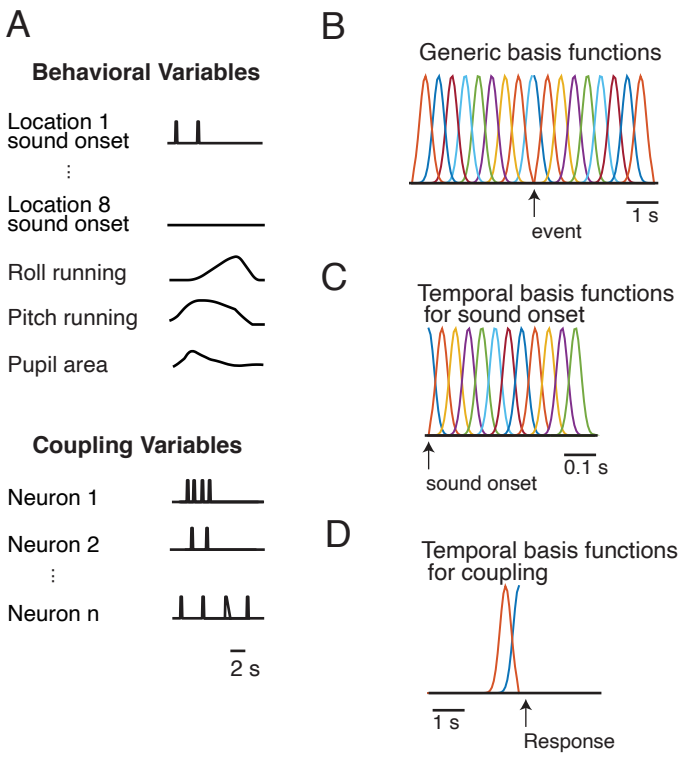

Figure S4: Construction of the predictors used in the encoding models. (A) Behavioral variables and coupling variables used in variants of the Generalized Linear Models (GLMs) to relate neural activity to behavioral variables and/or activity of other simultaneously imaged neurons. Coupling variables could be either Non-SOM neurons or SOM neurons. (B) Depiction of basis functions used to allow for modeling the temporal relationship between behavioral and/or coupling variables to neural activity. The variables in A were convolved with a set of basis functions moving either forward or backward in time, depending on the type of variable. For example, running velocity in each possible direction was deconvolved with eight basis functions stretching 1 s in time, prospectively and retrospectively. Thus eight total predictors for each running velocity direction were included in the model. (C) Schematic of the basis functions convolved with sound onset times, for each possible sound location. These spread only forward in time from sound onset. (D) Basis functions convolved with each coupling variable (each simultaneously imaged neuron).

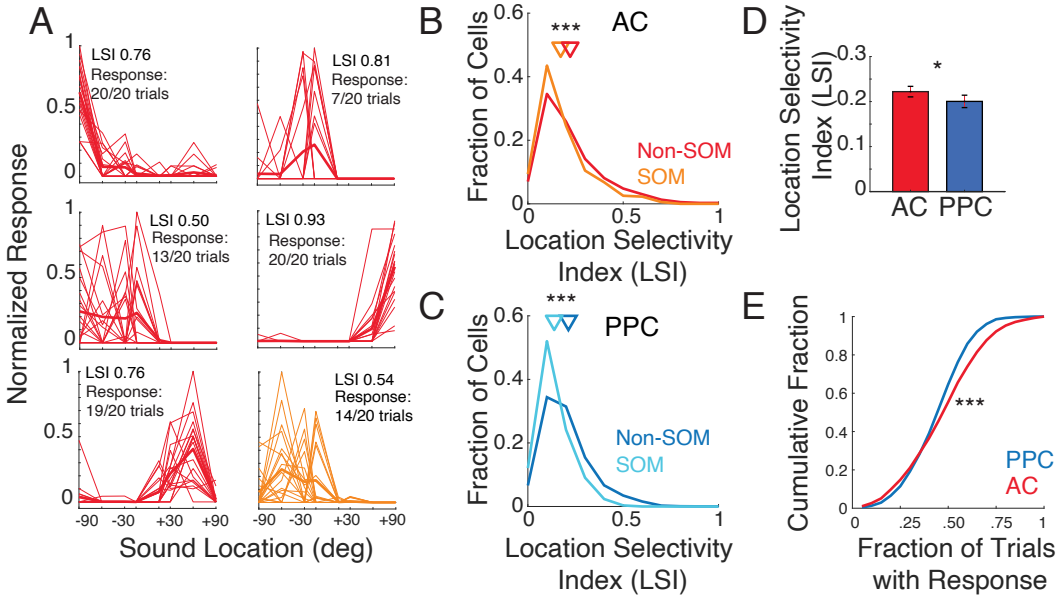

Figure S5: Sound Location Selectivity in AC and PPC. (A) Six example neurons with diverse sound location preferences, ranging from ipsilateral (-90 - 0 degrees) to contralateral locations (0 - +90 degrees). Thin lines: mean response during sound presentation of individual trials. Thick lines: Trial average. The location selectivity index (LSI) and response reliability are reported for each example cell. Red: Example Non-SOM neurons. Orange: Example SOM neuron. (B) Distribution of Location Selectivity Index (LSI) for Non-SOM (N=2455) and SOM (N=354) neurons in AC. Triangles indicate population means. (C) As in B, for PPC (Non-SOM N=2553; SOM N=298). (D) Mean location selectivity index in AC and PPC. (E) Cumulative distributions of response reliability, the fraction of sound-responsive trials, in AC and PPC. * $p<0.05$, ***$p<0.001$, error bars indicate SEM. Full summary of values and statistics in Tables S7-8.

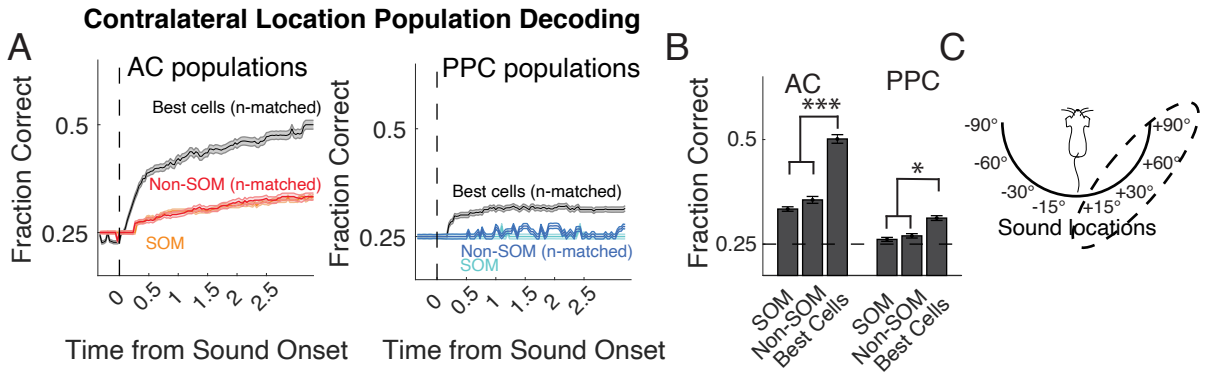

Figure S6: Decoding Sound Location from SOM and Non-SOM Population Activity. (A) As in Figure 4C, but when classifying specific contralateral locations. Chance performance is .25, as there are four possible contralateral locations. (B) As in Figure 4D, but when classifying within contralateral locations. Dotted line indicates chance performance. (C) The discrimination being performed by the decoder, classifying each trial as one of four possible locations on the contralateral side. *** $p<0.001$, * $p<0.05$. See Table S9 for full statistics.

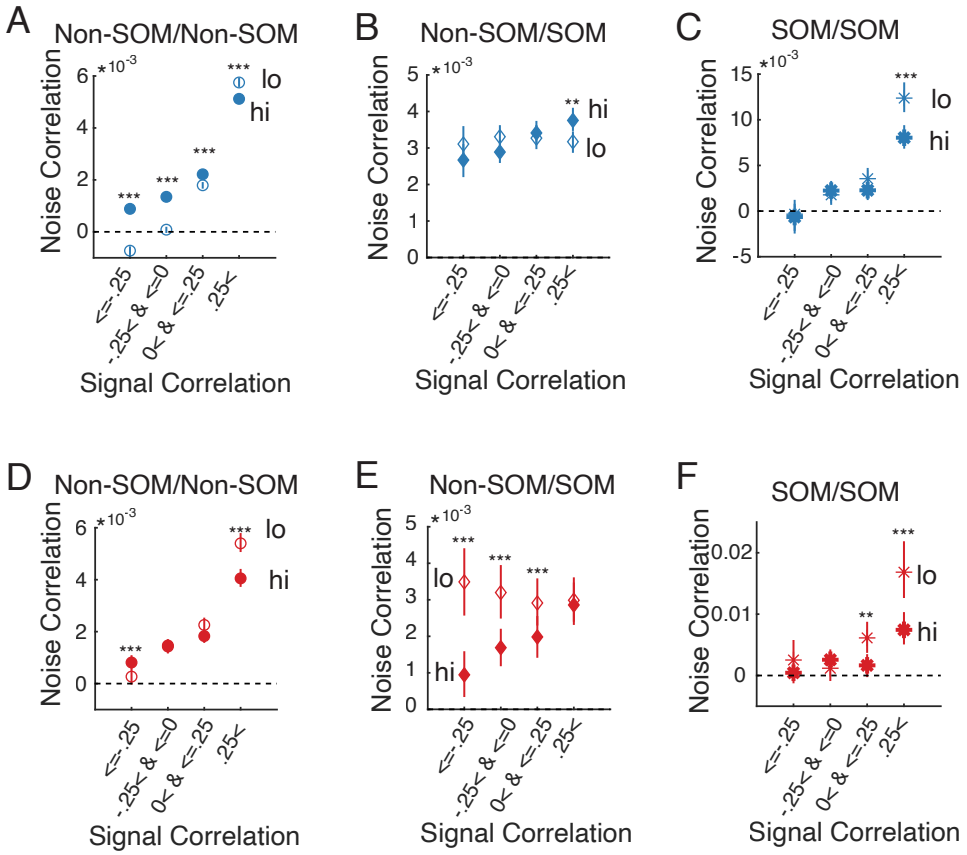

Figure S7: Noise correlations tended to be weaker in high arousal states, but the magnitude of the effect depended on signal correlation and cell type. (A) Mean pairwise noise correlation of Non-SOM/Non-SOM neurons in PPC datasets, binned by signal correlation. Filled circles: high arousal, open circles: low arousal. High and low arousal were defined as in Figure 2, by clustering pupil area measurements across the imaging session. Bin 1, N=92989; Bin 2, N=192997; Bin 3, N=181712; Bin 4, N=152621. (B) As in A, for Non-SOM/SOM pairs in PPC datasets. Filled diamonds: high arousal, open diamonds: low arousal. Bin 1, N= 19046; Bin 2, N=39303; Bin 3, N=37849; Bin 4, N=33121. (C) As in A, for SOM/SOM pairs in PPC datasets. Bolded stars: high arousal, Unbolded stars: low arousal. Bin 1, N=984; Bin 2, N=2412; Bin 3; N=2277; Bin 4, N=1971. (D-F) As in A-C, for AC datasets. Error bars: bootstrapped 95% confidence intervals around the mean. ***p<0.001, **p<0.01, permutation test. Full summary of values and statistics in Table S11.

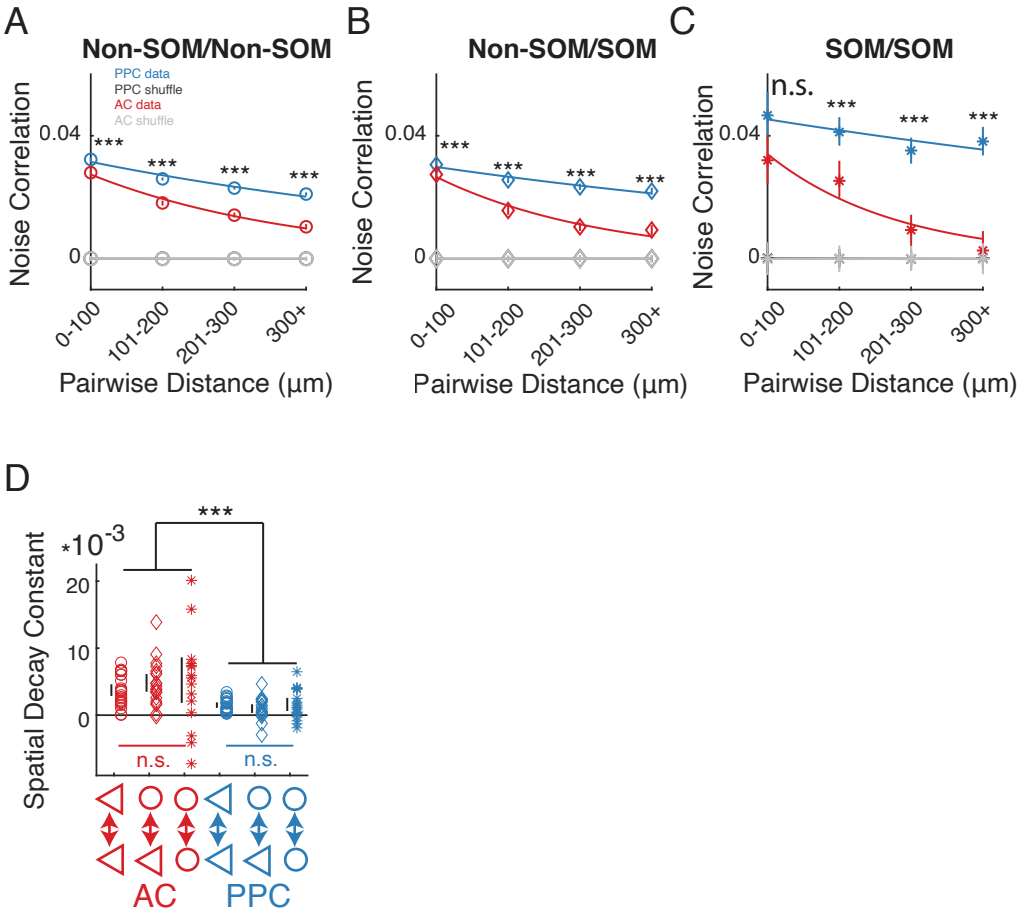

Figure S8: The Spatial Scale of Correlated Variability Differs in AC and PPC, Measured in Running Bout "Trials". (A-D) As in Figure 5D-G, but noise correlations were measured based on responses during running bouts (defined as in Figure 2) as trials in the spontaneous context, rather than on sound stimulus trials in passive listening. Overall trends in noise correlations based on running bouts were similar to those based on sound stimulus responses. Full summary of values and statistics in Tables S14-16.

Table S1: Comparing Pupil Diameter and Running Speed in AC and PPC Datasets

Group	N	Mean	Standard Deviation	95% Confidence Interval of the Mean	p value (unpaired permutation test)
AC datasets mean cm/s, passive	24	31.5	33.4	21.8-51.3	.20
PPC datasets, mean cm/s, passive	20	20.5	15.5	15.2-27.8	
AC datasets mean cm/s, spontaneous	24	17.7	12.8	13.5-23.6	.52
PPC datasets mean cm/s, spontaneous	20	15.4	9.1	12.2-19.5	
AC datasets mean pupil diameter, passive	24	.39	.12	.35-.44	.43
PPC datasets mean pupil diameter, passive	20	.36	.096	.32-.41	
AC datasets mean pupil diameter, spontaneous	24	.33	.073	.31-.36	.73
PPC datasets mean pupil diameter, spontaneous	20	.33	.10	.29-.38	
AC datasets, pupil dilations min^{-1}	24	1.0	.52	.82-1.2	.65
PPC datasets, pupil dilations min^{-1}	20	.94	.40	.78-1.1	
AC datasets, running bouts min^{-1}	24	.87	.57	.66-1.1	.59
PPC datasets, running bouts min^{-1}	20	.97	.70	.72-1.4	
AC datasets, fraction time high cluster passive	24	.36	.20	.29-.45	.54
PPC datasets, fraction time high cluster passive	20	.32	.17	.25-.40	

AC datasets fraction time high cluster, spontaneous	24	.23	.15	.18-.29	.47
PPC datasets fraction time high cluster, spontaneous	20	.26	.17	.20-.37	
AC datasets fraction time running >15 cm/s passive	24	.31	.20	.25-.40	.43
PPC datasets fraction time running >15 cm/s passive	20	.27	.16	.20-.34	
AC datasets fraction time running >15 cm/s spontaneous	24	.21	.13	.16-.26	.65
PPC datasets fraction time running >15 cm/s spontaneous	20	.22	.13	.17-.28	

Table S2: Comparing activity during high and low arousal periods during spontaneous context

Group	N	Mean	Standard Deviation	95% Confidence Interval of the Mean	p value
PPC Non-SOM norm. FR, high arousal	4719	.24	.20	.21-.28	
PPC Non-SOM norm. FR, low arousal	4719	.13	.11	.11-.17	
Paired permutation					0.00
PPC SOM norm. FR, high arousal	525	.30	.24	.25-.34	
PPC SOM norm. FR, low arousal	525	.14	.12	.11-.17	
Paired permutation					0.00
AC Non-SOM norm. FR, high arousal	2645	.20	.15	.17-.24	
AC Non-SOM norm. FR, low arousal	2645	.18	.12	.15-.21	
Paired permutation					0.00
AC SOM norm. FR, high arousal	359	.20	.22	.17-.24	
AC SOM norm. FR, low arousal	359	.17	.14	.15-.22	
Paired permutation					.0029
AC SOM arousal modulation index[1]	359	.057	.29	.027-.085	
AC Non-SOM, arousal modulation index[2]	2645	.035	.28	.025-.046	
PPC Non-SOM arousal modulation index[3]	4719	.25	.31	.24-.26	
PPC SOM arousal modulation index[4]	525	.35	.31	.32-.37	

Kruskal Wallis[1-4]	7.2E-12
Unpaired permutation[1,2]	.22
Unpaired permutation[,1,3]	<.00010
Unpaired permutation[,2,3]	<.00010
Unpaired permutation[,1,4]	<.00010
Unpaired permutation[,2,4]	<.00010
Unpaired permutation[,3,4]	<.00010

Table S3: Correlation coefficients with pupil diameter and running speed during spontaneous context

Group	N	Mean	Standard Deviation	95% Confidence Interval of the Mean	p value
AC Non-SOM, pupil correlation coefficient[1]	2645	.0057	.033	.0045-.0070	
AC SOM pupil correlation coefficient[2]	359	.0091	.031	.0061-.12	
PPC Non-SOM pupil correlation coefficient[3]	4719	.035	.043	.034-.036	
PPC SOM pupil correlation coefficient[4]	525	.055	.049	.051-.059	
Kruskal Wallis[1-4]					6.3E-250
Unpaired permutation[1,2]					.063
Unpaired permutation[,1,3]					<.00010
Unpaired permutation[,2,3]					<.00010
Unpaired permutation[,1,4]					<.00010
Unpaired permutation[,2,4]					<.00010
Unpaired permutation[,3,4]					<.00010
AC Non-SOM, running speed correlation coefficient[1]	2645	.0020	.034	.00060-.0033	
AC SOM running speed correlation coefficient[2]	359	.0048	.034	.0013-.0089	
PPC Non-SOM running speed correlation coefficient[3]	4719	.033	.044	.032-.034	
PPC SOM running speed correlation coefficient[4]	525	.057	.055	.053-.062	
Kruskal Wallis[1-4]					0.00
Unpaired permutation[1,2]					.15
Unpaired permutation[,1,3]					<.00010
Unpaired permutation[,2,3]					<.00010
Unpaired permutation[,1,4]					<.00010
Unpaired permutation[,2,4]					<.00010
Unpaired permutation[,3,4]					<.00010

Table S4: Comparing activity during high and low arousal periods during passive listening context

Group	N	Mean	Standard Deviation	95% Confidence Interval of the Mean	p value
PPC Non-SOM norm. FR, high arousal	4719	.20	.20	.18-.33	
PPC Non-SOM norm. FR, low arousal	4719	.14	.17	.11-.26	
Paired permutation					0.00
PPC SOM norm. FR, high arousal	525	.24	.22	.20-.30	
PPC SOM norm. FR, low arousal	525	.15	.20	.11-.22	
Paired permutation					0.00
AC Non-SOM norm. FR, high arousal	2645	.18	.13	.15-.22	
AC Non-SOM norm. FR, low arousal	2645	.15	.12	.13-.19	
Paired permutation					0.00
AC SOM norm. FR, high arousal	359	.17	.13	.15-.22	
AC SOM norm. FR, low arousal	359	.14	.12	.12-.18	
Paired permutation					0.00
AC Non-SOM, arousal modulation index[1]	2645	.072	.26	.063-.083	
AC SOM arousal modulation index[2]	359	.079	.28	.049-.11	
PPC Non-SOM arousal modulation index[3]	4719	.18	.29	.17-.19	
PPC SOM arousal modulation index[4]	525	.26	.28	.24-.29	
Kruskal Wallis[1-4]					2.1E-66
Unpaired permutation[1,2]					.63
Unpaired permutation[,1,3]					<.00010
Unpaired permutation[,2,3]					<.00010

Unpaired permutation[,1,4]	<.00010
Unpaired permutation[,2,4]	<.00010
Unpaired permutation[,3,4]	<.00010

Table S5: Correlation coefficients with pupil diameter and running speed during passive listening context

Group	N	Mean	Standard Deviation	95% Confidence Interval of the Mean	p value
AC Non-SOM, pupil correlation coefficient[1]	2645	.0096	.031	.0081-.010	
AC SOM pupil correlation coefficient[2]	359	.010	.033	.0074-.014	
PPC Non-SOM pupil correlation coefficient[3]	4719	.030	.042	.029-.031	
PPC SOM pupil correlation coefficient[4]	525	.043	.044	.038-.046	
Kruskal Wallis[1-4]					5.3E-115
Unpaired permutation[1,2]					.63
Unpaired permutation[,1,3]					<.00010
Unpaired permutation[,2,3]					<.00010
Unpaired permutation[,1,4]					<.00010
Unpaired permutation[,2,4]					<.00010
Unpaired permutation[,3,4]					<.00010
AC Non-SOM, running speed correlation coefficient[1]	2645	.0067	.029	.0056-.0078	
AC SOM running speed correlation coefficient[2]	359	.0076	.30	.0050-.011	
PPC Non-SOM running speed correlation coefficient[3]	4719	.029	.042	.028-.030	
PPC SOM running speed correlation coefficient[4]	525	.045	.047	.038-.046	
Kruskal Wallis[1-4]					1.2E-146
Unpaired permutation[1,2]					.59
Unpaired permutation[,1,3]					<.00010
Unpaired permutation[,2,3]					<.00010
Unpaired permutation[,1,4]					<.00010
Unpaired permutation[,2,4]					<.00010
Unpaired permutation[,3,4]					<.00010

Table S6: Pupil and Running Contributions, from Encoding Model in Figure 3

Group	n	Mean	Standard Deviation	95% Confidence Interval of the Mean	p value
AC Non-SOM, pupil diameter contribution[1]	2476	0.0027	0.0086	0.0023-0.0031	
AC SOM, pupil diameter contribution[2]	330	0.0036	0.0123	0.0025-0.0049	
PPC Non-SOM, pupil diameter contribution[3]	4525	0.0029	0.0060	0.0028-0.0031	
PPC SOM, pupil diameter contribution[4]	505	0.0034	0.0059	0.0029-.0040	
Kruskal Wallis[1-4]					<0.0001
Unpaired permutation[1,2]					0.0780
Unpaired permutation[,1,3]					0.1259
Unpaired permutation[,2,3]					0.2360
Unpaired permutation[,1,4]					0.0619
Unpaired permutation[,2,4]					0.9520
Unpaired permutation[,3,4]					0.1070
AC Non-SOM, running speed correlation coefficient[1]	2476	0.0020	0.0050	0.0019-0.0023	
AC SOM running speed correlation coefficient[2]	330	0.0023	0.0005	0.0019-0.0320	
PPC Non-SOM running speed correlation coefficient[3]	4525	0.0079	0.0156	0.0075-0.0083	
PPC SOM running speed correlation coefficient[4]	505	0.0113	0.0181	0.0099-0.0131	
Kruskal Wallis[1-4]					<0.0001
Unpaired permutation[1,2]					0.4409
Unpaired permutation[,1,3]					0.0001
Unpaired permutation[,2,3]					0.0001
Unpaired permutation[,1,4]					0.0001
Unpaired permutation[,2,4]					0.0001
Unpaired permutation[,3,4]					0.0002

Table S7: Location Selectivity Index

Group	N	Mean	Standard Deviation	95% Confidence Interval of the Mean	p value
AC All Neurons[1]	2809	0.20	0.16	0.19 – 0.21	<0.01
PPC All Neurons[2]	2851	0.19	0.12	0.18 – 0.19	
AC Non-SOM[3]	2455	0.20	0.16	0.20 – 0.21	<0.001
AC SOM[4]	354	0.16	0.13	0.15 – 0.18	
PPC Non-SOM[5]	2553	0.20	0.12	0.19 – 0.20	<0.001
PPC SOM[6]	298	0.13	0.09	0.12 – 0.14	
Kruskal Wallis[3-6]					<0.0001
Unpaired permutation[3,4]					<0.001
Unpaired permutation[3,5]					<0.05
Unpaired permutation[3,6]					<0.0001
Unpaired permutation[4,5]					<0.0001
Unpaired permutation[4,6]					<0.0001
Unpaired permutation[5,6]					<0.0001

Table S8: Sound Response Reliability

	N	Mean	Standard Deviation	95% Confidence Interval of the Mean	p value
AC All Neurons[1]	2809	0.49	0.20	0.49 – 0.50	<0.0001
PPC All Neurons[2]	2851	0.46	0.15	0.46 – 0.47	
AC Non-SOM[3]	2455	0.49	0.20	0.49 – 0.50	
AC SOM[4]	354	0.50	0.19	0.48 – 0.51	
PPC Non-SOM[5]	2553	0.46	0.15	0.45 – 0.47	
PPC SOM[6]	298	0.48	0.14	0.46 – 0.49	
Kruskal Wallis[3-6]					<0.0001
Unpaired permutation[3,4]					0.808
Unpaired permutation[3,5]					<0.0001
Unpaired permutation[3,6]					0.149
Unpaired permutation[4,5]					<0.0001
Unpaired permutation[4,6]					0.132
Unpaired permutation[5,6]					0.143

Table S9: Sound Location Decoding

Group	n	Mean	Standard Deviation	95% Confidence Interval of the Mean	p value
AC Best Cells – LR[1]	24 x 10	0.86	0.11	0.85-0.87	
AC Non-SOM – LR[2]	24 x 10	0.68	0.13	0.66-0.69	
AC SOM – LR[3]	24 x 10	0.68	0.12	0.66-0.69	
PPC Best Cells – LR[4]	20 x 10	0.65	0.10	0.64-0.67	
PPC Non-SOM – LR[5]	20 x 10	0.53	0.09	0.52-0.53	
PPC SOM – LR[6]	20 x 10	0.52	0.09	0.51-0.53	
Kruskal Wallis[1-6]					0.0001
Unpaired permutation[1,2]					0.0001
Unpaired permutation[1,3]					0.0001
Unpaired permutation[1,4]					0.0001
Unpaired permutation[1,5]					0.0001
Unpaired permutation[1,6]					0.0001
Unpaired permutation[2,3]					0.8167
Unpaired permutation[2,4]					0.1189
Unpaired permutation[2,5]					0.0001
Unpaired permutation[2,6]					0.0001
Unpaired permutation[3,4]					0.1160
Unpaired permutation[3,5]					0.0001
Unpaired permutation[3,6]					0.0001
Unpaired permutation[4,5]					0.0001
Unpaired permutation[4,6]					0.0001
Unpaired permutation[5,6]					0.4644
AC High Arousal – LR (All cells)	24 x 10	0.83	0.16	0.81-0.85	0.0003
AC Low Arousal – LR (All cells)	24 x 10	0.78	0.12	0.76-0.80	
PPC High Arousal – LR (All cells)	20 x 10	0.54	0.13	0.53-0.55	0.0600
PPC Low Arousal – LR (All cells)	20 x 10	0.57	0.13	0.56-0.59	

AC Best Cells – Contra[1]	24 x 10	0.44	0.13	0.45-0.48	
AC Non-SOM – Contra[2]	24 x 10	0.32	0.10	0.33-0.35	
AC SOM – Contra[3]	24 x 10	0.31	0.09	0.32-0.34	
PPC Best Cells – Contra[4]	20 x 10	0.28	0.09	0.26-0.30	
PPC Non-SOM – Contra[5]	20 x 10	0.26	0.08	0.25-0.27	
PPC SOM – Contra[6]	20 x 10	0.25	0.09	0.25-0.27	
Kruskal Wallis[1-6]					<0.0001
Unpaired permutation[1,2]					<0.0001
Unpaired permutation[1,3]					<0.0001
Unpaired permutation[1,4]					<0.0001
Unpaired permutation[1,5]					<0.0001
Unpaired permutation[1,6]					<0.0001
Unpaired permutation[2,3]					0.5082
Unpaired permutation[2,4]					0.9354
Unpaired permutation[2,5]					<0.0001
Unpaired permutation[2,6]					<0.0001
Unpaired permutation[3,4]					0.116
Unpaired permutation[3,5]					<0.0001
Unpaired permutation[3,6]					<0.0001
Unpaired permutation[4,5]					0.0121
Unpaired permutation[4,6]					0.0118
Unpaired permutation[5,6]					0.9354

Table S10: Pairwise Noise Correlations (Sound Location Trials)

Group	N	Mean	Standard Deviation	95% Confidence Interval of the Mean	p value
AC all neurons[1]	204502	.026	.054	.026-.026	
PPC all neurons[2]	757282	.035	.070	.035-.035	
Unpaired permutation[1,2]					<.00010
AC Non-SOM/Non-SOM[3]	160241	.026	.053	.025-.026	
AC Non-SOM/SOM[4]	41473	.026	.055	.025-.026	
AC SOM/SOM[5]	2788	.033	.067	.030-.035	
Kruskal Wallis[3-5]					.00021
Unpaired permutation[3,4]					.83
Unpaired permutation[4,5]					<.00010
Unpaired permutation[3,5]					<.00010
PPC Non-SOM/Non-SOM[6]	620319	.033	.068	.033-.033	
PPC Non-SOM/SOM[7]	129319	.040	.073	.040-.041	
PPC SOM/SOM[8]	7644	.071	.10	.069-.073	
Kruskal Wallis[6-8]					0.00
Unpaired permutation[6,7]					<.00010
Unpaired permutation[7,8]					<.00010
Unpaired permutation[6,8]					<.00010
Kruskal Wallis[1-8]					0.00

Table S11: High Noise Correlation – Low Noise Correlation

Group	N	Mean	Standard Deviation	95% Confidence Interval of the Mean	p value (paired permutation test, α=.0125)
AC Non-SOM/Non-SOM bin 1, high arousal	11349	.00081	.014	.00054-.0011	.0056
AC Non-SOM/Non-SOM bin 1, low arousal	11349	.00027	.017	-.000039-.00058	
AC Non-SOM/Non-SOM bin 2, high arousal	16401	.0015	.016	.0012-.0017	.82
AC Non-SOM/Non-SOM bin 2, low arousal	16401	.0014	.017	.0012-.0017	
AC Non-SOM/Non-SOM bin 3, high arousal	16039	.0018	.018	.0016-.0021	.022
AC Non-SOM/Non-SOM bin 3, low arousal	16039	.0023	.018	.0020-.0025	
AC Non-SOM/Non-SOM bin 4, high arousal	18326	.0041	.024	.0037-.0044	0.00
AC Non-SOM/Non-SOM bin 4, low arousal	18326	.0054	.025	.0051-.0058	
AC Non-SOM/SOM bin 1, high arousal	3190	.00094	.018	.00034-.0016	0.00
AC Non-SOM/SOM bin 1, low arousal	3190	.0035	.026	.0012-.0022	
AC Non-SOM/SOM bin 2, high arousal	4401	.0017	.018	.0012-.0022	0.00
AC Non-SOM/SOM bin 2, low arousal	4401	.0032	.024	.0025-.0040	
AC Non-SOM/SOM bin 3, high arousal	4113	.0020	.019	.0014-.0026	0.00

AC Non-SOM/SOM bin 3, low arousal	4113	.0029	.021	.0023-.0036	.80
AC Non-SOM/SOM bin 4, high arousal	4819	.0029	.020	.0023-.0035	.23
AC Non-SOM/SOM bin 4, low arousal	4819	.0030	.021	.0024-.0036	
AC SOM/SOM bin 1, high arousal	208	.00046	.012	-.0013-.0020	.29
AC SOM/SOM bin 1, low arousal	208	.0025	.022	-.0012-.0058	
AC SOM/SOM bin 2, high arousal	298	.0026	.014	.0010-.0042	.0026
AC SOM/SOM bin 2, low arousal	298	.0012	.018	-.00089-.0033	
AC SOM/SOM bin 3, high arousal	235	.0017	.015	-.00026-.0035	.0002
AC SOM/SOM bin 3, low arousal	235	.0061	.020	.0037-.0088	
AC SOM/SOM bin 4, high arousal	372	.0074	.024	.0051 -.010	0.00
AC SOM/SOM bin 4, low arousal	372	.017	.046	.013 - .022	
PPC Non-SOM/Non-SOM bin 1, high arousal	24940	.00088	.015	.00071 - .0011	0.00
PPC Non-SOM/Non-SOM bin 1, low arousal	24940	-.00073	.013	-.00089 – -.00056	
PPC Non-SOM/Non-SOM bin 2, high arousal	50964	.0013	.016	.0012 - .0015	0.00
PPC Non-SOM/Non-SOM bin 2, low arousal	50964	.000083	.014	-.000043 - .00019	
PPC Non-SOM/Non-SOM bin 3, high arousal	54231	.0022	.017	.0021-.0024	0.00

PPC Non-SOM/Non-SOM bin 3, low arousal	54231	.0018	.015	.0017-.0019	
PPC Non-SOM/Non-SOM bin 4, high arousal	46853	.0051	.020	.0049-.0053	0.00
PPC Non-SOM/Non-SOM bin 4, low arousal	46853	.0057	.020	.0056-.0059	
PPC Non-SOM/SOM bin 1, high arousal	4636	.0027	.015	.0022-.0031	.15
PPC Non-SOM/SOM bin 1, low arousal	4636	.0031	.017	.0027-.0036	
PPC Non-SOM/SOM bin 2, high arousal	9860	.0029	.016	.0026-.0032	.058
PPC Non-SOM/SOM bin 2, low arousal	9860	.0033	.017	.0030-.0036	
PPC Non-SOM/SOM bin 3, high arousal	11477	.0034	.017	.0031-.0037	.50
PPC Non-SOM/SOM bin 3, low arousal	11477	.0033	.017	.0030-.0036	
PPC Non-SOM/SOM bin 4, high arousal	11049	.0038	.018	.0035-.0041	.0061
PPC Non-SOM/SOM bin 4, low arousal	11049	.0032	.016	.0029-.0035	
PPC SOM/SOM bin 1, high arousal	241	-.00065	.012	-.0022-.00080	.78
PPC SOM/SOM bin 1, low arousal	241	-.00034	.015	-.0025-.0012	
PPC SOM/SOM bin 2, high arousal	539	.0022	.013	.0011-.0033	.53
PPC SOM/SOM bin 2, low arousal	539	.0018	.013	.00068-.0027	
PPC SOM/SOM bin 3, high arousal	667	.0023	.015	.0012-.0035	.11
PPC SOM/SOM bin 3, low arousal	667	.0035	.015	.0025-.0047	

PPC SOM/SOM bin 4, high arousal	788	.0080	.018	.0068-.0094	0.00
PPC SOM/SOM bin 4, low arousal	788	.012	.023	.011-.014	

Table S12: Pairwise Noise Correlations Binned By Distance (Sound Location Trials)

Group	N	Mean	Standard Deviation	95% Confidence Interval of the Mean	p value (unpaired permutation test, α=.0125)
AC Non-SOM/Non-SOM bin 1	27224	.042	.070	.041-.043	.39
PPC Non-SOM/Non-SOM bin 1	92989	.041	.076	.041-.042	
AC Non-SOM/Non-SOM bin 2	50252	.027	.053	.026-.027	<<.00010
PPC Non-SOM/Non-SOM bin 2	192997	.034	.069	.034-.034	
AC Non-SOM/Non-SOM bin 3	46293	.020	.046	.019-.020	<<.00010
PPC Non-SOM/Non-SOM bin 3	181712	.031	.066	.031-.032	
AC Non-SOM/Non-SOM bin 4	36472	.19	.044	.019-.020	<<.00010
PPC Non-SOM/Non-SOM bin 4	152621	.029	.064	.029-.030	
AC Non-SOM/SOM bin 1	6755	.044	.071	.042-.046	.0092
PPC Non-SOM/SOM bin 1	19046	.047	.079	.046-.048	
AC Non-SOM/SOM bin 2	13384	.027	.055	.027-.028	<<.00010
PPC Non-SOM/SOM bin 2	39303	.040	.073	.040-.041	
AC Non-SOM/SOM bin 3	12334	.020	.049	.019-.021	<<.00010
PPC Non-SOM/SOM bin 3	37849	.038	.071	.038-.039	
AC Non-SOM/SOM bin 4	9000	.018	.046	.017-.019	<<.00010
PPC Non-SOM/SOM bin 4	33121	.039	.072	.038-.040	
AC SOM/SOM bin 1	513	.058	.086	.051-.066	.00050

PPC SOM/SOM bin 1	984	.078	.11	.071-.085	
AC SOM/SOM bin 2	891	.036	.066	.032-.041	<.00010
PPC SOM/SOM bin 2	2412	.074	.11	.070-.078	
AC SOM/SOM bin 3	830	.025	.061	.021-.029	<.00010
PPC SOM/SOM bin 3	2277	.066	.10	.063-.070	
AC SOM/SOM bin 4	554	.016	.045	.012-.020	<.00010
PPC SOM/SOM bin 4	1971	.071	.10	.067-.076	

Table S13: Noise Correlation Spatial Decay Constants (Sound Location Trials)

Group	N	Mean	Standard Deviation	95% Confidence Interval of the Mean	p value
AC all Λ[1]	71	.0041	.0037	.0033-.0050	
PPC all Λ[2]	59	.00079	.0014	.0005-.0012	
Unpaired permutation[1,2]					<.00010
AC Non-SOM/Non-SOM Λ[3]	24	.0035	.0018	.0028-.0042	
AC SOM/Non-SOM Λ[4]	24	.004	.0023	.0031-.0049	
AC SOM/SOM Λ[5]	23	.0049	.0057	.0028-.0073	
Kruskal Wallis[3-5]					.61
PPC Non-SOM/Non-SOM Λ[6]	20	.00092	.00070	.00070-.0013	
PPC SOM/Non-SOM Λ[7]	20	.00047	.001	-.00011-.00055	
PPC SOM/SOM Λ[8]	19	.00098	.0021	.00030-.0022	
Kruskal Wallis[6-8]					.47
Kruskal Wallis[3-8]					1.96E-09

Table S14: Pairwise Noise Correlations (Running Bout Trials)

Group	N	Mean	Standard Deviation	95% Confidence Interval of the Mean	p value
AC all neurons[1]	204502	.016	.089	.016-.017	
PPC all neurons[2]	757282	.025	.11	.025-.025	
Unpaired permutation[1,2]					<.00010
AC Non-SOM/Non-SOM[3]	160241	.017	.090	.016-.017	
AC Non-SOM/SOM[4]	41473	.015	.084	.014-.015	
AC SOM/SOM[5]	2788	.017	.084	.014-.020	
Kruskal Wallis[3-5]					.10
PPC Non-SOM/Non-SOM[6]	620319	.025	.11	.024-.025	
PPC Non-SOM/SOM[7]	129319	.025	.10	.024-.025	
PPC SOM/SOM[8]	7644	.039	.11	.037-.042	
Kruskal Wallis[6-8]					2.39E-41
Unpaired permutation[6,7]					.82
Unpaired permutation[7,8]					<.00010
Unpaired permutation[6,8]					<.00010
Kruskal Wallis[3-8]					6.3E-225

Table S15: Pairwise Noise Correlations Binned By Distance (Running Bout Trials)

Group	N	Mean	Standard Deviation	95% Confidence Interval of the Mean	p value (unpaired permutation test, α=.0125)
AC Non-SOM/Non-SOM bin 1	27224	.028	.10	.027-.029	<.00010
PPC Non-SOM/Non-SOM bin 1	92989	.032	.12	.031-.033	
AC Non-SOM/Non-SOM bin 2	50252	.018	.091	.017-.019	<.00010
PPC Non-SOM/Non-SOM bin 2	192997	.026	.11	.025-.026	
AC Non-SOM/Non-SOM bin 3	46293	.014	.087	.013-.015	<.00010
PPC Non-SOM/Non-SOM bin 3	181712	.023	.11	.022-.023	
AC Non-SOM/Non-SOM bin 4	36472	.010	.084	.0095-.011	<.00010
PPC Non-SOM/Non-SOM bin 4	152621	.021	.11	.020-.022	
AC Non-SOM/SOM bin 1	6755	.027	.093	.025-.030	<.00010
PPC Non-SOM/SOM bin 1	19046	.031	.11	.029-.032	
AC Non-SOM/SOM bin 2	13384	.016	.085	.014-.017	<.00010
PPC Non-SOM/SOM bin 2	39303	.026	.10	.025-.027	
AC Non-SOM/SOM bin 3	12334	.010	.080	.0091-.012	<.00010
PPC Non-SOM/SOM bin 3	37849	.023	.10	.022-.024	

AC Non-SOM/SOM bin 4	9000	.0094	.079	.0076-.011	<.00010
PPC Non-SOM/SOM bin 4	33121	.022	.10	.021-.023	
AC SOM/SOM bin 1	513	.032	.094	.024-.040	.017
PPC SOM/SOM bin 1	984	.047	.12	.040-.054	
AC SOM/SOM bin 2	891	.025	.092	.020-.032	<.00010
PPC SOM/SOM bin 2	2412	.041	.11	.037-.046	
AC SOM/SOM bin 3	830	.0094	.075	.0041-.014	<.00010
PPC SOM/SOM bin 3	2277	.035	.10	.031-.039	
AC SOM/SOM bin 4	554	.0027	.066	-.0026-.0090	<.00010
PPC SOM/SOM bin 4	1971	.038	.10	.034-.043	

Table S16: Noise Correlation Spatial Decay Constants (Running Bout Trials)

Group	N	Mean	Standard Deviation	95% Confidence Interval of the Mean	p value
AC all λ[1]	71	.0037	.0045	.0027-.0048	
PPC all λ[2]	59	.0011	.0017	.0007-.0015	
Unpaired permutation[1,2]					<.00010
AC Non-SOM/Non-SOM λ[3]	24	.0030	.0026	.0020-.0042	
AC SOM/Non-SOM λ[4]	24	.0038	.0037	.0023-.0054	
AC SOM/SOM λ[5]	23	.0047	.0072	.0013-.0082	
Kruskal Wallis[3-5]					.93
PPC Non-SOM/Non-SOM λ[6]	20	<.00010	.0013	.00038-.0015	
PPC SOM/Non-SOM λ[7]	20	<.00010	.0014	.00048-.0017	
PPC SOM/SOM λ[8]	19	.0012	.0024	.00028-.0023	
Kruskal Wallis[6-8]					.57
Kruskal Wallis[3-8]					.00092

Table S17: Coupling

Group	N	Mean	Standard Deviation	95% Confidence Interval of the Mean	p value
AC Non-SOM/Non-SOM[1]	2428	0.0017	0.0057	0.0015-0.0020	
AC Non-SOM/SOM[2]	320	0.0019	0.0057	0.0015-0.0027	
AC SOM/SOM[3]	327	0.0037	0.0112	0.0027-0.0052	
PPC Non-SOM/Non-SOM[4]	4048	0.0031	0.0112	0.0028-0.0035	
PPC Non-SOM/SOM[5]	485	0.0022	0.0101	0.0033-0.0051	
PPC SOM/SOM[6]	484	0.0074	0.0193	0.0058-0.0092	
Kruskal Wallis[1-6]					<0.0001
Unpaired permutation[1,2]					<0.0001
Unpaired permutation[1,3]					<0.0001
Unpaired permutation[1,4]					<0.0001
Unpaired permutation[1,5]					<0.0001
Unpaired permutation[1,6]					<0.0001
Unpaired permutation[2,3]					<0.0001
Unpaired permutation[2,4]					<0.0001
Unpaired permutation[2,5]					<0.0001
Unpaired permutation[2,6]					<0.0001
Unpaired permutation[3,4]					<0.0001
Unpaired permutation[3,5]					<0.0001
Unpaired permutation[3,6]					<0.0001
Unpaired permutation[4,5]					<0.0001
Unpaired permutation[4,6]					<0.0001
Unpaired permutation[5,6]					<0.0001